

THE PENNSYLVANIA STATE UNIVERSITY
SCHREYER HONORS COLLEGE

DEPARTMENT OF BIOENGINEERING

INVESTIGATING THE MECHANICS OF CANCER CELL MEMBRANES USING
MICROFLUIDICS

KHALIL RAMADI
SPRING 2014

A thesis
submitted in partial fulfillment
of the requirements
for baccalaureate degrees in
Bioengineering and Mechanical Engineering
with honors in Bioengineering

Reviewed and approved* by the following:

Siyang Zheng
Assistant Professor of Bioengineering
Thesis Supervisor

William Hancock
Professor of Bioengineering
Honors Adviser

Peter Butler
Associate Professor of Bioengineering
Thesis Reader

* Signatures are on file in the Schreyer Honors College.

ABSTRACT

The study of circulating tumor cells (CTCs) has been at the forefront of cancer research in recent years. CTC isolation and characterization can yield significant insight into the type of tumor in question and its progression with treatment. A primary method of CTC isolation relies on their distinctive mechanical properties compared to other blood cells. Namely, CTCs have been found to be larger and more deformable than white blood cells, their closest counterparts in blood. However, no holistic mechanical model describing these behaviors exists. In order to better design CTC isolation technologies, the dynamics of different cell types as they expanded were studied and compared. Cancer cells were found to expand significantly, much more than the elasticity of the cell membrane would normally allow. We hypothesize that this is due to the presence of membrane folds that flatten out as the cell expands. We used microfluidics and hypotonic pressure to expand the cells and MATLAB image processing to analyze the response. Finally, we mapped the results to the equivalent dynamic behavior of a Kelvin-Voigt viscoelastic material. We also modeled the osmotic pressure gradient influence on expansion over time. Our findings support the feasibility of using mechanical differences to improve CTC isolation and characterization in microfluidic devices. Cancer cells were significantly larger and more deformable than peripheral blood mononuclear cells. Moreover, it was found that different cancer cells exhibit unique expansion dynamics, suggesting a possible avenue for phenotyping unknown tumor cells.

TABLE OF CONTENTS

List of Figures	iii
List of Tables	iv
Acknowledgements.....	v
Introduction.....	1
Chapter 1 Materials and Methods	12
Cell lines and cell culture protocol	12
FICOLL blood fractionation	13
In Situ Cell Imaging and Analysis	14
Microfluidic Device Design.....	16
Microfluidic device fabrication.....	18
Protocol for cell manipulation using microfluidic device.....	20
Microfluidic Device Testing	21
Chapter 2 Results	23
H661 Expansion Curves.....	25
MCF7 Expansion Curves	27
MNC Expansion Curves	29
Chapter 3 Analysis of Results.....	35
Kelvin-Voight Viscoelastic Model	36
Osmotic Pressure Driving Force Model.....	43
Chapter 4 Discussion	54
Chapter 5 Conclusion.....	61
Chapter 6 Appendices	64
Appendix A: Image Analysis MATLAB Code.....	64
Appendix B: Cell Expansion Images	70
Bibliography.....	72

LIST OF FIGURES

Figure 1. Cancer metastasis mechanism highlighting the role played by EMT and MET transitions. Adapted from Ref: (Harouaka, Nisic, & Zheng, 2013).....	4
Figure 2. Common techniques used to measure cell mechanical properties. Taken from Ref: (Di Carlo, 2012).....	7
Figure 3. Microfluidic device for testing. The device was used to transfer cells instantaneously from isotonic 1x PBS to pure DI water and image their subsequent expansion.	17
Figure 4. Microfluidic device junction joint between 2 fluid inputs. The blue liquid is flowing in the from the bottom while the clear liquid is flowing in from the right. The 2 then meet at a 90° junction, although they do not mix due to the low Reynolds number.	21
Figure 5. Separation region of microfluidic device. Fluid flow in the main channel is from left to right. The main channel contains 2 co-flowing liquids, one dyed blue and one clear. The blue liquid is filtered out by means of the side channels running upwards in this picture.....	22
Figure 6. Percentage expansion of each of the 3 cell types studied, compared to the initial diameter. T-tests confirmed p-values <0.0001, implying a significant difference in % expansion between each of the cell subpopulations. Also, there is no correlation found between % expansion and initial diameter.	24
Figure 7. Survival plots for each of the 3 cell types tested. Also shown is the percentage of cells that remain intact by the end of the viewing period. Mantel-Cox Test yielded p<0.0001 for all 3 comparisons, thus each cell type is significantly different from the others tested.....	24
Figure 8. H661 expansion curve for all cells imaged, with diameter measured (µm) vs. time elapsed (sec). The mean of all diameters at each time point was plotted, N=53.	25
Figure 9. H661 Expansion curve of Diameter (µm) vs. Time (Sec). There are 2 plots, differentiating between cells that burst (n=31) and those that remain intact n=22). The data at the first 3 time points at t = 0, 30, and 60 seconds are significantly different (**: p<0.01, *: p<0.05). The mean of all diameters at each time point was plotted.....	26
Figure 10. Representative MCF7 expansion curve for all cells imaged, Diameter (µm) vs. Time (sec). The mean of all diameters at each time point was plotted. (n _{total} = 132)	27
Figure 11. Representative MCF7 expansion curves of Diameter (µm) vs. Time (sec). There are 2 plots, differentiating cells that burst (n=13) and those that do not (n=28). The 2 subpopulations are not significantly different, with the minimum p-value of 0.6271 occurring at t = 690 seconds.	28

Figure 12. MNC expansion curve for all cells imaged, Diameter (μm). Vs. Time (sec). The mean of all diameters at each time point was plotted. (n=48)	29
Figure 13. MNC Expansion curves of Diameter (μm) vs Time (sec). There are 2 plots for 2 cell subpopulations: those that burst (n=31) and those that remain intact (n=17).	30
Figure 14. MNC expansion curves of Diameter (μm) vs. Time (Sec). Shown are 2 possibly distinct groups of cells, those with initial diameter larger than 10 μm , and those with initial diameter less than 10 μm . T-tests reveal a significant difference between the small (n=33) and large (n=15) data points, suggesting that the MNCs consisted of 2 subpopulations.	31
Figure 15. MNC expansion curves of Diameter (μm) vs. Time (Sec). The MNC cell population is divided into 4 distinct subgroups. Although some significant difference is seen, it is not enough to warrant dividing the MNC group into 4 subpopulations: 2 subpopulations of small and large are sufficient.	32
Figure 16. Representative expansion curves of Diameter (μm) vs. (Time (Sec) for each cell type plotted on same set of axes. Due to the statistical different between the 2 sets of MNC data shown in figure 14, the MNC data was divided into 2 subpopulations.	33
Figure 17. % expansion curve of MCF7, H661, small MNCs, and large MNCs. Expansion is measured relative to the mean cell diameter at time = 0 seconds, before being immersed in hypotonic solution.	34
Figure 18. Kelvin-Voight viscoelastic material model. The model consists if an elastic spring and a linear damping element placed in parallel.	36
Figure 19. H661 % Expansion plot with viscoelastic model curve fit. The dashed red lines represent a 95% confidence interval in the curve fit.	37
Figure 20. MCF7 % Expansion with viscoelastic model curve fit. The dashed red lines represent a 95% confidence interval in the curve fit.	38
Figure 21. Small and large MNCs % expansion with viscoelastic model curve fit to each. The dashed red lines represent a 95% confidence interval in the curve fits.	39
Figure 22. Comparison of % expansion of MCF7, H661, Small MNCs, and Large MNCs. Also shown are the curve fits for each data set according to a viscoelastic model.	40
Figure 23. Viscoelastic curve fits for MCF7, H661, Small MNCs, and Large MNCs.	41
Figure 24. MCF7 % Expansion with osmotic pressure driving force model curve fit. The dashed red lines represent a 95% confidence interval in the curve fit.	47
Figure 25. H661 % Expansion with osmotic pressure driving force model curve fit. The dashed red lines represent a 95% confidence interval in the curve fit.	48

Figure 26. Small and Large MNCs % Expansion with osmotic pressure driving force model curve fits for each. The dashed red lines represent a 95% confidence interval in the curve fits.....	49
Figure 27. % Expansion of MCF7, H661, Small MNCs, and Large MNCs. Also shown are the osmotic pressure driving force model curve fits to each.....	50
Figure 28. MCF7, H661, Small MNCs, and Large MNCs osmotic pressure driving force model curve fits.....	51
Figure 29. Viscoelastic model (solid curves) and osmotic pressure driving force model (dashed curves) curve fits for MCF7, H661, Small MNCs, and Large MNCs.....	53

LIST OF TABLES

Table 1. Table showing values of constants for viscoelastic model curve fits.	42
Table 2. Values for constants in the total strain equation for the osmotic pressure driving force model. The values reflect the equation of the curve fit plotted to each set of data.	52

ACKNOWLEDGEMENTS

First and foremost, I would like to thank my thesis advisor, Dr. Siyang Zheng, for the opportunity to immerse myself in such a multidisciplinary project, exposing and allowing me to learn about everything from cell culture techniques to microfabrication. Throughout my research he has been a source of infinite ideas and advice, and a fantastic mentor, always keeping the project on track and looking for new exciting avenues to explore. I'm sure I would not be in a position to write this were it not for him.

Also, I would still be far behind in my work if it wasn't for the helping hands I've had along the way. I would like to thank Mingda Zhou, Ramdane Harouaka, and Tim (Yin-Ting) Yeh in the MiniBio lab for making me feel so welcome in the lab and for always being willing to help out and give advice whenever I was having trouble with my experiments. I would also like to thank Sijie Hao, also of the MiniBio lab, for his help in designing and building the microfluidic devices. Finally, my thanks to Merissa Nisic and Waleed Khan for their help in maintaining cancer cell lines.

Introduction

The battle against cancer has been a long and arduous one, starting even before the National Cancer Act in 1971 and still very much ongoing today. It has grown to be one of the toughest battles to be fought in modern medicine, with cancer proving to be a particularly difficult disease to treat or cure. Part of this difficulty is due to the diversity of development stages that cancers undergo. However, the uniting factor among these cancers is their eventual progression to metastasis. Malignant cancers originate in a particular organ or system and proceed to spread to other parts of the body. This process is known as metastasis, and is driven by unregulated cell division. (Kufe et al., 2003)

Metastases cause 90% of all human cancer deaths (Mehlen & Puisieux, 2006), and are considered a turning point in the cancer development of a patient. Metastasis, involving the spread of invasive tumors to different parts of the body, prevents the possibility of a focused, localized treatment such as radiation therapy or surgical removal, forcing the patient to resort to whole-body treatments such as chemotherapy. Thus, the mortality rate of pre-metastatic cancer patients is significantly less than that of metastatic patients. The current belief in cancer treatment is the belief that early detection offers the best possibility for cure. Hence, there has been an increasing push towards developing technologies and means to detect cancers early on, without resorting to incidental findings of large tumors through routine body scans.

One of these methods is the study of circulating tumor cells (CTCs). In the last decade, the study of CTCs has been at the forefront of research. CTCs have been found to be a principal mechanism of metastases, whereby they are shed by the primary tumor into the bloodstream,

settling down and forming secondary tumors in other locations downstream. The detection of CTCs in the blood can serve as a powerful diagnostic tool to assess the stage of progression of a cancer in a patient (Lin, Balic, Zheng, Datar, & Cote, 2011). It can also be a method of cancer detection, if the primary tumor has not been discovered. Finally, the characterization and analysis of these cells can yield information about the type of tumor in question, its genetics, and invasiveness without having to resort to invasive biopsies. The hope is that not only will CTC analysis be a tool in cancer treatment and management, but also an assay routinely used in blood analysis of regular healthy patient check ups, enabling early detection of malignant tumors.

Characterization of CTCs can be achieved through their capture from a blood sample and subsequent enrichment. However, CTCs are rare cells in the blood, especially compared to the population of other cells types, such as white blood cells (monocytes, lymphocytes, granulocytes) and erythrocytes. Studies estimate their population to be a mere one cell per billion normal blood cells in metastatic (Maheswaran & Haber, 2010). In healthy or non-metastatic patients, the number of CTCs in blood will be even less. Thus, the advantages of CTCs can only be reaped if adequate detection and isolation technologies are developed.

Over the last 6 years, an overwhelming number of novel technologies for CTC capture have been reported. The majority of these have made use of microfluidic devices for this purpose. A microfluidic device makes use of extremely small (μL or less) volumetric flow rates and low Reynolds number flow for precise manipulation of small particles or cells. A landmark report was published in 2007 describing a microchip that separated CTCs using both hydrodynamics and antibody expression (Nagrath et al., 2007). The microchip consisted of an array of microposts coated with anti-epithelial cell adhesion molecules (EpCAM) antibodies. The specific flow patterns around the posts were simulated under different flow rates to determine the optimal scenario for micropost-cell contact and attachment. This device was reported to have successfully

captured CTCs in 99% of metastatic cancer patient blood samples with 50% purity. This group's efforts have culminated with the development of the FDA-cleared CellSearch™ system.

Since then, other similar immune-based assays have been developed for CTC isolation. For example, Hoshino et al. made use of magnetic nanoparticles functionalized with anti-EpCAM antibodies that bind to CTCs expressing EpCAM (Hoshino et al., 2011). A magnetic sweeper (MagSweep) device has also been proposed, which separates circulating cancer epithelial cells from whole blood also using EpCAM antigens binding to magnetic nanoparticles (Talasaz et al., 2009).

The problem with using an epithelial marker to capture CTCs arises due to the epithelial to mesenchymal transition (EMT). Cancer cells that successfully intravasate into the bloodstream often undergo EMT, altering their phenotype and improving their ability to metastasize to different sites of the body (Kalluri & Weinberg, 2009). The reverse process, a mesenchymal-to-epithelial transition (MET), occurs once the cells have successfully spread to another location. It has been demonstrated that EMT is a direct indicator of the metastatic potential of cancer cells, and correlates with disease prognosis (Yamada et al., 2013). Mesenchymal phenotype CTCs, however, lose their expression of EpCAM (by definition, an epithelial marker) and so can evade capture by the very immunoassays designed to catch CTCs (Nagrath et al., 2007). Hence, other approaches to CTC capture need to be developed.

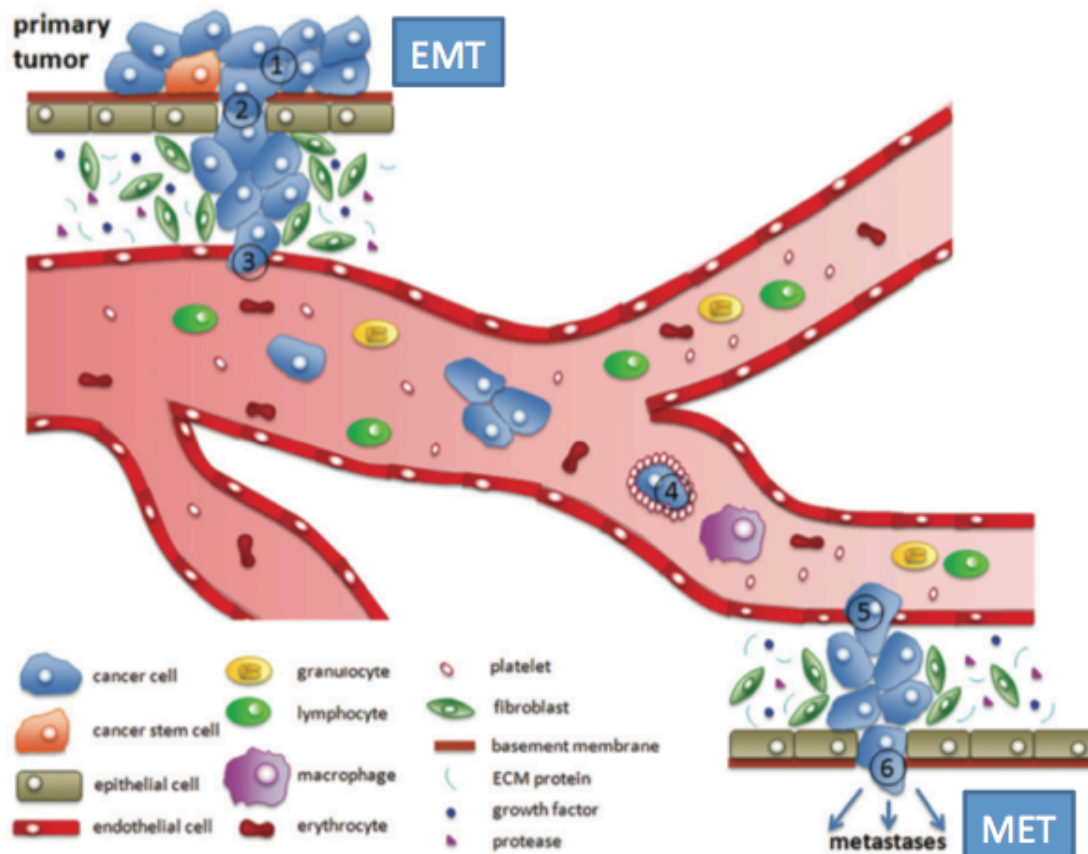


Figure 1. Cancer metastasis mechanism highlighting the role played by EMT and MET transitions. Adapted from Ref: (Harouaka, Nisic, & Zheng, 2013)

The need for a label-free method of CTC detection has given rise to a plethora of mechanics-based separation techniques. In blood, cancer cells are most similar to white blood cells (WBCs), and so characterizing differences in the dynamical mechanical responses between these two cell populations is essential to a working mechanical separation mechanism. Cancer cells have been shown to have different mechanical characteristics compared to other cells present in circulating blood (Hou et al., 2009). Specifically, they have been shown to be larger, more deformable, and able to survive greater stresses than WBCs (Suresh, 2007). It should be noted that mechanical differences do arise from the EMT. In keeping with the findings that

mesenchymal CTCs have greater metastatic potential, they have also been found to be stiffer and more mechanically rigid than epithelial phenotype CTCs.

A mechanical assay for CTC isolation also offers distinct advantages over biochemical means of separation. The assay is often simpler, requiring no reagents or trained technicians to perform. This not only makes the assay easier to complete, but also allows point-of-care measurements. Since mechanical assays are simpler, they often take quicker time to conclude, which is beneficial to time-sensitive clinical scenarios. Finally, the lack of human interaction with the assay assures repeatability and consistency, eliminating the possibility of discrepant results due to human error (Di Carlo, 2012).

Microfluidic devices have been reported that separate CTCs from a blood sample by taking advantage of these unique mechanical properties. One example of this is a PDMS device a 2-dimensional array of funnel ratchets. A steady flow in the x-direction is coupled with an oscillatory flow in the y-direction, pushing the cells in and out of the ratchets. Only those that are relatively small are able to pass through, leaving the larger CTCs separated from the rest of the blood (McFaul, Lin, & Ma, 2012). Another popular technique has relied on inertial microfluidics. That is, particles of different size and mechanical properties have different equilibrium positions when passed through a channel, as a result of the balance between lift and buoyancy forces (Ho & Leal, 1974). It should be noted that weight can usually be neglected in force analyses in microfluidic flow, since capillary action and viscous forces dominate at such low Reynolds numbers.

Inertial migration has been utilized in different ways to separate CTCs from whole blood. One study used deterministic lateral displacement, whereby different size particles travel in different paths along a maze of obstacles (Huang, Cox, Austin, & Sturm, 2004). Another built on

the concept of inertial migration by designing a microfluidic device where particle's lateral equilibrium position would not only depend on their size, but also on their viscoelastic properties (Hur, Henderson-MacLennan, McCabe, & Di Carlo, 2011). Hur et al. succeeded in separating CTCs based on their distinct viscoelastic properties. It was found that the cells accurately mimicked the behavior of viscous droplets in immiscible flow instead of rigid particles. The advantages of such techniques are that they are inherently passive. They require no active external factor to be applied other than a pressure gradient to drive the flow through the device.

It is clear then that the mechanics of cells is a commonly used characteristic for separation and has been studied previously. The cellular mechanics have been studied using various analytical techniques including atomic force microscopy (AFM), micropipette aspiration, and optical stretching. Leeka et al. used AFM to compare normal and malignant human bladder cells. They found that cancer cells were 10 times less stiff than their normal counterparts, as measured by the Young's modulus of each. AFM uses a finely tuned cantilevered beam that is pushed down onto the surface to be studied by a focused light beam. The deflection of the cantilever then depends on the stiffness of the substrate. Another group also used AFM and found a similar result, that cancer cells appeared to be inherently less stiff and more deformable (Cross, Jin, Rao, & Gimzewski, 2007). This group also suggested the level of decrease in stiffness correlates with an increase in the metastatic potential of a cancer cell, arguing that decreased stiffness increases the likelihood of successful invasion of new tissue. However, various studies have differed on whether it is a decrease in stiffness or in deformability that correlates with increased malignancies. One study found that stiffness of cancer cells increases after chemotherapy, suggesting that the stiffer cells have a selective survival advantage (Suresh, 2007). It is likely that the EMT/MET play a role in this discrepancy and that depending on the cell's immediate surroundings an increase or decrease in stiffness may be appropriate. For example, an

extravasating cell might find it beneficial to be more flexible and less stiff. In any case, for the purpose of the studies here, we focus mainly on the deformability of different cells, and to a much lesser extent, their stiffness.

Dielectrophoretic field-flow fractionation (dFFF) was used in other studies to study both the deformability of cells as well as the membrane capacitance. dFFF is a microfluidic implementation of dielectrophoresis, whereby a particle is subjected to a varying (non-uniform) electric field. The behavior of the particles as they pass through the electric field reveals the mechanical force balance, which can be manipulated using a model to obtain mechanical characteristics of the particles. They found, again, that cancer cells were much more deformable than healthy cells (Shim, Gascoyne, Noshari, & Hale, 2011). A piezoresistive microcantilever was used by Shim et al. to test the different dynamic response of MCF7 (human cancer cell line) and MCF10A (human epithelial normal cell line) cells. They found a 20% difference in the deformability of the 2 cell lines at certain loading frequencies, with MCF7 cells having greater deformability. Across all the loading frequencies tested, MCF7 cells were found to be less stiff.

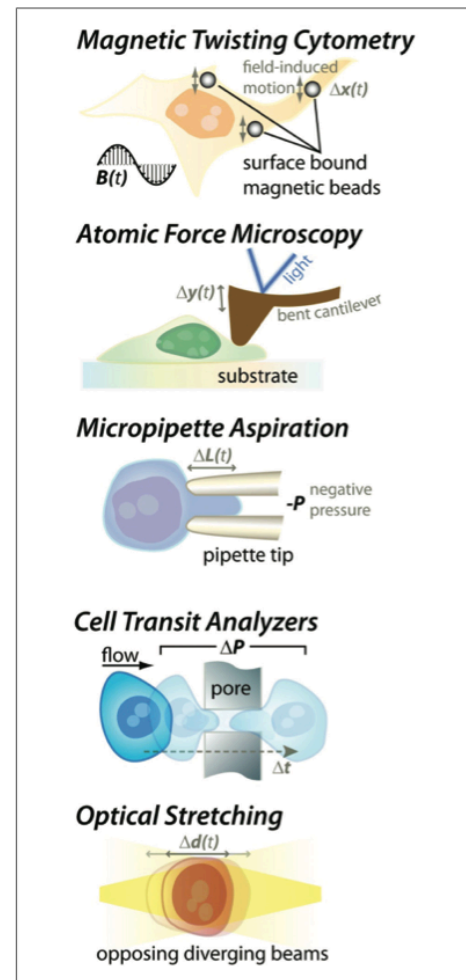


Figure 2. Common techniques used to measure cell mechanical properties. Taken from Ref: (Di Carlo, 2012)

Micropipette aspiration uses a pipette to apply a negative pressure to a portion of the cell. The cell deforms and is partially sucked into the pipette tip. The extent to which the cell manages

to deform and enter the tip can then be correlated with the pressure (or stress) applied to characterize cell stiffness (Hochmuth, 2000). A microfluidic device implementation of this forces cells through a narrow pore (Hou et al., 2009). The cells again have to deform in order to pass through the opening. Using the known value of the hydrodynamic pressure gradient and the time elapsed for a single cell to transit the narrow opening, mechanical characteristics such as deformability can be calculated. This study again found that MCF7 cells elongated more, and hence were more deformable than healthy human cells. A similar device was proposed and tested with red blood cells (RBCs), whereby the pressure drop across the channel was monitored in real-time along with imaging to record the cell deformation ((Abkarian, Faivre, & Stone, 2006). This information could be used to re-construct the dynamic behavior of the cells during deformation.

Put together, all these techniques have given us remarkable insight into the mechanical properties of different cancer and healthy cells. However, we still fail to have a holistic mechanical model that can adequately describe cellular dynamics. Part of the reason for this is the complex interactions between the cell membrane and cytoskeleton that determine the mechanical behavior of the cell (Fletcher & Mullins, 2010). A significant aspect of cell expansion that is seldom studied in isolation is the phenomenon of membrane folding. Cells have often been observed to deform, stretch, and expand in ways beyond what would be expected. An example of this is neutrophil phagocytosis, when a neutrophil engulfs a foreign particle or debris to destroy it. The neutrophil membrane undergoes substantial structural changes in order to do this successfully (Murphy et al., 2011). Another example is B cell differentiation into Plasma cells. This transformation occurs when foreign antigens are detected, and allow large quantities of antibodies to be produced quickly. In this process however, B cells undergo substantial volumetric expansion, expanding in diameter from an average of 5 μm to 10 μm . A doubling of the diameter inherently implies a 4-fold increase in the surface area (Wang, Castro, & Boyce, 2011).

There have been studies describing the process of ‘blebbing’. Blebs are portions of the membrane that have detached from the cytoskeleton, and thus expand outside the cell, projecting the membrane surface in a certain direction. This behavior has been observed in a variety of situations, and was first identified in apoptotic cells (Robertson et al. 1978). More recently, tumor cells have been observed to use blebbing as a means for motility to escape chemotherapy treatments *in vivo*, especially those that target cell matrix inhibition (Friedl et al., 2003). Tumor cells have also been observed to use blebbing to invade new tissues (Voura et al., 1998). Hence, this phenomenon has been studied in the context of apoptosis, cytokinesis, and tumor cell behavior, but not in terms of cell expansion and membrane folding. Blebs are an appropriate example of how ‘hidden’ membrane surface area can be advantageous to cells. (Charras & Paluch, 2008).

The elasticity of the plasma membrane in RBCs has been previously studied using micropipette aspiration (Mohandas & Evans, 1994). These studies found that the membrane could only experience a strain of 5% before rupture. The plasma membrane is essentially identical in most cells, from RBCs to WBCs and CTCs, consisting predominantly of a phospholipid bilayer. Hence, membrane elasticity alone could not explain the large expansions undergone by neutrophils and B cells. In order to explain this, the theory of membrane folding has been proposed and has since been confirmed experimentally by scanning electron microscopy (SEM) (Schmid-Schönbein, Shih, & Chien, 1980). Cells are able to expand to such a huge extent due to ‘hidden’ surface area present in the membrane in the form of microscopic surface wrinkles and folds. This is also advantageous to cells because it increases their surface area-to-volume ratio, which eases signaling to other nearby cells by having a larger area over which to communicate. Models hypothesizing the cytoskeletal interactions with the plasma membrane to bring about this folding-unfolding mechanism have also been proposed (Hallett & Dewitt, 2007).

The current techniques and models of CTC and WBC mechanics do not take this phenomenon into account. In addition, these methods only measure the mechanics of a single portion of the cell membrane, and extrapolate the findings to represent the membrane in its entirety. While this might be a reasonable assumption to make for a uniform substrate, the presence of folds and wrinkles can introduce substantial uncertainty in the mechanical characteristics of one portion of the membrane as opposed to another. What is lacking, then, is an overall model that is able to characterize the cell membrane mechanics in its entirety while taking into account both the phospholipid bilayer elasticity as well as wrinkles in the membrane. The studies outlined in this thesis strive to achieve such a model.

In order to characterize cell mechanics on a macro-cellular scale, it was necessary to establish a new means by which to stress the cells in a uniform manner. All the techniques described thus far selectively applied stress to a portion of the cell. It was decided that the ideal method of doing so would be to stretch the cell outwards, equally in all directions. The idea of manipulating osmolarity and tonicity of the surrounding solution cells relative to the cells was developed to achieve this. Water molecules diffuse freely through the phospholipid membrane, without the need of carriers or active transport. Therefore, placing cells in a hypotonic solution would cause water to rush through the membrane into the cell and apply an outward pressure on the membrane. While it is realized that an abundance of water might disrupt the nucleus, genetic information, and intracellular signaling cascades, it will leave the membrane unharmed. The membrane bilayer is composed of two rows of phospholipids, arranged so that the hydrophilic heads point outward towards the cytoplasm and extra-cellular matrix (ECM) while the hydrophobic tails point inwards, away from water-containing solutions. This is to our advantage, since water molecules will be unable to enter the bilayer and tamper with the resulting mechanical response characteristics until bursts. After bursting, the cell ceases to be significant

for this experiment, as the maximum stress able to be withstood by the membrane has been reached and passed. Furthermore, since our goal is to characterize the pure mechanics of the membrane of different cells, the disruption of other cellular assays is assumed to be relatively inconsequential.

The subsequent parts of this thesis will outline the experimental protocol followed in swelling the cells by placing them in a hypotonic solution, show the results of these experiments, and analyze and discuss the results and their implications to the context of CTC isolation and characterization.

Chapter 1

Materials and Methods

Cell lines and cell culture protocol

MCF7 (human breast cancer cell line) and H661 (human lung carcinoma cell line) were thawed and suspended in Dulbecco's modified eagle medium (DMEM), and placed in 10 ml cell culture flasks with fresh DMEM in a 1:4 ratio. Both cell lines grow adherent to the flask surface. Culture flasks were kept in the incubator at 37 °C, 5% CO₂ and were passed when they reach confluence (approximately twice per week). Cell confluence was verified by observing the flask under 10x light microscope.

When passing the cells from one flask to another, all media and supplements were first warmed in a water bath to 37 °C in order to avoid shocking the cells. To pass the adherent cells, the medium in the flask was first aspirated. The flask was then rinsed once with 5ml of 1x phosphate buffered saline (PBS). The PBS was then aspirated and 1.5ml of Trypsin added, in order to detach the cells from the bottom of the flask. The flask was placed in the incubator for 1-2 minutes or until the cells were visibly detached, as observed under an inverted microscope. To deactivate the trypsin, 8ml of DMEM was added to flask and mixed well to ensure no cell clumps remained.

A new flask containing 6ml of DMEM was meanwhile prepared. 1-2 ml of cell suspension was added to this flask, after which it was placed in the incubator until the cells again

reached confluence. The remaining cells in suspension were used for the experiments outlined in the protocols below.

FICOLL blood fractionation

Healthy donor blood was used to obtain white blood cells (WBCs) for experimentation. Mononuclear WBCs were extracted using Ficoll-Paque PLUS (GE Healthcare Bio-Sciences, Pittsburg, PA) following manufacturer's protocol. The protocol used was adapted from the manufacturer's protocol instruction, #71-7167-00-AG as detailed below.

A blood sample was diluted with 1x PBS in a 1:1 ratio. Ficoll (3 ml) was placed in a 15ml centrifuge tube. Diluted blood (4ml) was then carefully added on top of the Ficoll, such that the blood was layered and did not mix with the Ficoll. The tube was centrifuged at 400 x g for 35 minutes.

This results in a separation of the individual components of blood according to density. The plasma remains at the top, followed by a thin layer of mononuclear cells (lymphocytes and monocytes) and platelets. Below this is the Ficoll and at the very bottom the erythrocytes and granulocytes sediment. The top plasma layer was first carefully extracted using a pipette. A clean pipette was then used to extract the mononuclear cell layer, which was subsequently suspended in 6ml 1x PBS. This cell suspension was centrifuged again at 100 x g for 10 minutes. The supernatant was removed, and the cells re-suspended in 3ml 1x PBS.

In Situ Cell Imaging and Analysis

Cells were placed in a 15ml tube and centrifuged at 1500rpm for 5 minutes (Eppendorf Centrifuge 5430 R). The supernatant was aspirated and the cells re-suspended in 1x PBS.

A hemocytometer (Bright-Line™, Sigma-Aldrich, St. Louis, MO) was used to image the cell expansion process. An aliquot of cell suspension (10 µl) was placed in the hemocytometer using a pipette and observed under the microscope. A particular group of cells was selected and focused on. Without moving the hemocytometer or adjusting any settings, 100 µl of de-ionized water (DI H₂O) was added to the cells in the hemocytometer. Using programmed CapturePro imaging software, the cells were imaged at consistent time intervals for a given period of time. Before this process was repeated, the hemocytometer and cover slip were rinsed well with ethanol and wiped dry.

There was a concern that adding a large volume of water to the cell solution within the thin space between the hemocytometer and the cover slip would inhibit immersing the cells in the water. This was addressed by using food coloring-dyed water and 1x PBS. 10 ul of 1x PBS was initially placed in the hemocytometer. 100 ul of colored water was then quickly added using a pipette. It was clearly observed that very little mixing occurred between the 2 solutions. The only mixing observed was some diffusion that could be seen at the interface of the 2 liquids. However, the colored water quickly flooded the hemocytometer, immersing the viewing area and pushing the 1x PBS outside of the viewing area. Thus, cells that remained within the imaging area were fully immersed in DI H₂O, validating the process. Images were then analyzed using ImageJ software and custom MATLAB scripts. For the image processing, it was assumed that all cells

were not flattened in any way, and were treated as spheres. This assumption was justified by comparing the distance between the hemocytometer and the cover slip (100um) with the maximum cell diameter imaged (around 50um). We determined that there was enough extra space to warrant the assumption of cells being spherical.

Microfluidic Device Design

Preliminary results suggested that a significant portion of the expansion process takes place soon after immersing the cells in a hypotonic solution. This initial expansion was specifically noted in RBCs and WBCs, which can withstand substantially less stress than can CTCs. To investigate the veracity of this, we designed and fabricated a microfluidic device that enabled imaging of the cells instantaneously as they were passed from their isotonic suspension to a hypotonic solution. For the majority of our experiments, cells were passed from 1x phosphate buffered saline (1x PBS) to pure de-ionized (DI) water.

The Reynolds number is a property of a flowing fluid defined as the ratio of inertial forces to viscous forces in the given flow:

$$Re = \frac{\rho V D}{\mu}$$

Where ρ is the density of the fluid, V is the average mainstream velocity within the channel, D is the hydraulic diameter of the channel, and μ is the dynamic viscosity of the fluid.

For most microfluidic channels, the microscale value of the diameter, D , in equation (1) will ensure the Reynolds number remains small ($Re \ll 1$). Viscous effects dominate in this flow regime, while inertial effects are negligible. This regime is often called Stokes or creeping flow. This property of microfluidic flow allows for fluid manipulation that cannot be achieved with larger scale flow. For example, 2 distinct fluids can flow side by side in a single channel without mixing, due to viscous forces. The microfluidic device designed here makes use of this by co-

flowing the cells in isotonic 1x PBS alongside the hypotonic solution. Then, the PBS is filtered out gradually through a series of side channels, leaving the cells suspended in DI water. The side channel geometry is specifically designed so that cells are not also filtered out. A small side channel dimension coupled with a large downstream resistance ensures that particles (in this case, cells) above a critical radius do not enter the side channel (Zheng, Liu, & Tai, 2008). Figure 2 shows the final fabricated microfluidic device. Diffusion between the 2 co-flowing fluids is negligible, due to the dominant viscous forces as well as the extremely small time scale that the 2 fluids remain in contact with each other (<1 second).

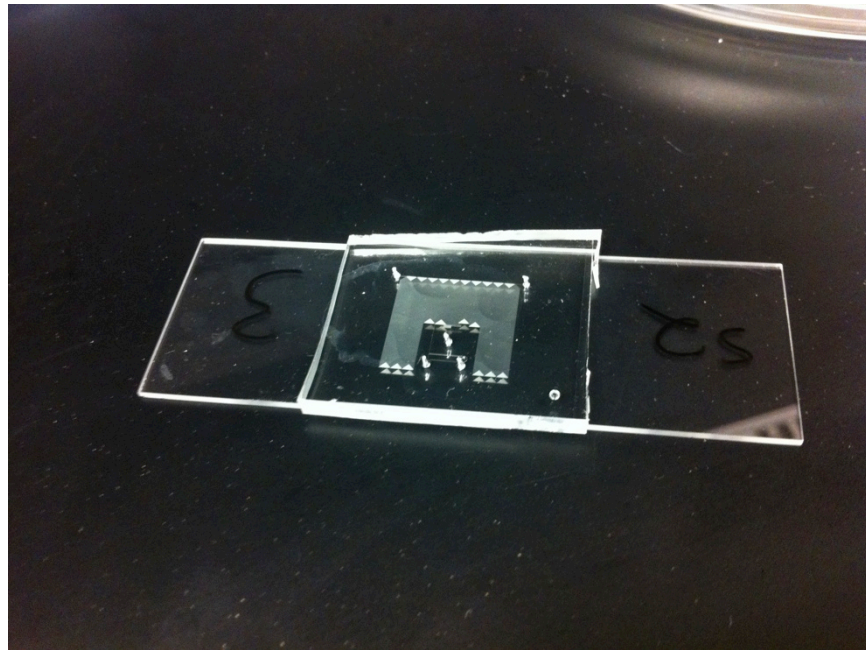


Figure 3. Microfluidic device for testing. The device was used to transfer cells instantaneously from isotonic 1x PBS to pure DI water and image their subsequent expansion.

Microfluidic device fabrication

The microfluidic device was first sketched on AUTOCAD. Photoplots of the device were obtained from FineLine Imaging (Colorado Springs, CO). Each photoplot contained 7 copies of the same pattern, to make full use of a single iteration of fabrication. These were used in patterning SU-8 Silicon wafers according to standard SU-8 photolithography procedures.

PDMS (Polydimethylsiloxane) parts A (Silicone elastomer base) and B (Silicone elastomer curing agent) were combined in a beaker in a ratio of 10:1. The mixture was whisked vigorously, producing air bubbles. To de-gas the mixture, the beaker was placed in a vacuum chamber for 10 minutes. Meanwhile, the Si wafer was primed with HMDS (hexamethyldisilazane) by placing the exposed wafer in a vacuum chamber with an open vial of HMDS for 3 minutes. This step prevents PDMS stiction to the mold, allowing it to be re-used multiple times.

The Si wafer was then placed in a Petri dish and de-gassed PDMS poured onto it. This was done as quickly as possible to prevent air bubbles from forming within the PDMS while it cured. The Petri dish was then covered and placed in an oven at 80 °C for 25 minutes. The PDMS will then have solidified and taken on the shape of the patterned wafer below it. The PDMS was carefully peeled off the wafer and then cut into separate blocks. This produced 7 distinct PDMS devices.

Holes were cut in the PDMS device inlets and outlets using 20 gauge Luer-stub adapters (BD Biosciences, Mountain View, CA). The PDMS blocks were then placed in a beaker containing IPA (Isopropyl alcohol), and placed in an ultrasonication bath for 5 minutes. Each

block was then removed from the solution, rinsed with acetone, rinsed with IPA, and nitrogen blow-dried. Glass slides to which the PDMS would be bonded were cleaned in a solution consisting of 140ml IPA, 70ml H₂O, and 3.5g KOH. The glass slides were left in this solution for 10 minutes, after which they were nitrogen dried. The glass slides were next treated with oxygen plasma and each PDMS block was placed on a single glass slide substrate, such that the patterned side was covered completely by the glass. These were then placed in an 80 °C oven for 4 hours, ensuring proper PDMS-glass bonding.

Protocol for cell manipulation using microfluidic device

The PDMS device was submerged in a beaker containing DI H₂O. The beaker containing the device and the water was then placed in a vacuum chamber for 20 minutes. Two 250 µl syringes (Hamilton, Reno, NV) were loaded with 1x PBS, connected to 20 gauge luer adapters (Hamilton, Reno, NV) and polypropylene tubing. Precision cut stainless steel tubes were inserted into the other ends of the tubing. 1x PBS is flushed through them, ensuring no bubbles remain. While the PDMS device remains submerged, the stainless steel tubes were inserted into the inlet ports. This ensures that no bubbles become entrapped in the syringe, tubing, or device channels. The device was then flushed with bovine serum albumin (BSA) in a similar fashion. BSA treats the PDMS channels, ensuring that cells and particles in the flow do not attach to the walls, potentially clogging the channel.

The cell (or bead) suspension placed in the syringes was density-balanced with Ficoll, to minimize cell settling within the flow and maintain a homogenous suspension. The syringes were placed in syringe pumps (Harvard Apparatus, Holliston, MA). The pumps were set to a flow rate of 1 µl/hr, at which point the subsequent flow through the channels was imaged for the desired time interval.

Microfluidic Device Testing

The initial expansion characteristics of MNCs were initially determined using a microfluidic device having 2 fluidic inputs, one with clear deionized water, and the other with DI water stained with food coloring. Figures 12 and 13 show the device running at a flow rate of 5ml/min for each of the 2 inputs. Figure 12 shows the point of junction between the 2 fluidic streams, and illustrates that the 2 fluids run in parallel, with minimal mixing before reaching the separation portion of the channel shown in figure 13. In experimental use, the blue stream would be the cell suspension in 1x phosphate buffered saline, while the clear stream would be DI water, as it is in this study. Figure 13 proves the device's efficacy in filtering out the colored water while keeping the clear water in the main channel.



Figure 4. Microfluidic device junction joint between 2 fluid inputs. The blue liquid is flowing in the from the bottom while the clear liquid is flowing in from the right. The 2 then meet at a 90° junction, although they do not mix due to the low Reynolds number.

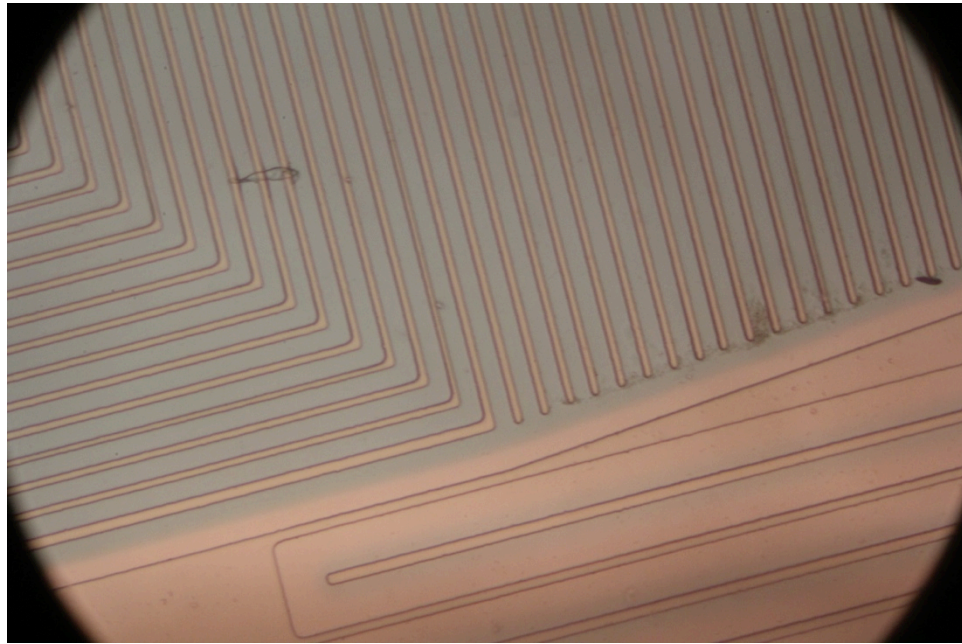


Figure 5. Separation region of microfluidic device. Fluid flow in the main channel is from left to right. The main channel contains 2 co-flowing liquids, one dyed blue and one clear. The blue liquid is filtered out by means of the side channels running upwards in this picture.

The device's effectiveness in not filtering out particles larger than the critical radius was then studied using fluorescent beads and microscopy. Spherical beads with diameter 10 μ m remained in the mainstream flow after passing through the separation region. Thus, assuming that cells behave as rigid spheres, we can assure that most of the MNCs and cancer cells of interest will likewise remain in the mainstream flow after passing through the separation region.

Chapter 2

Results

Studies were conducted on mononuclear cells (MNCs), MCF7, and H661 cells as outlined in the protocols section. Cells were placed in a hypotonic solution, and their subsequent expansion was imaged at fixed intervals of time. The images were analyzed using custom MATLAB code when possible (shown in Appendix A), and NIH ImageJ software. The diameter of each cell was measured frame-by-frame. The data depicted in Figures 6-17 were collected from a total of 132 MCF7 cells, 53 H661 cells, and 48 MNCs. Data obtained from microfluidic device testing was examined and determined to be indecisive. Not enough cells could be imaged adequately enough to allow for image processing. Furthermore, in those that were able to imaged no discernable increase in diameter could be seen. Thus, there was no significant jump in diameter in the seconds immediately following immersion of the cells in a hypotonic solution.

An end point analysis was first conducted, comparing the initial diameter of each of the different cell types, and the resulting percentage expansion undergone. Figure 6 shows this data for MNCs, H661, and MCF7 cell types. A survival plot, shown in figure 7, shows the percentage of the cells imaged from each cell type that remained intact and did not burst after a fixed amount of time. Mean dynamic expansion curves showing the diameter growth over time are shown in figures 8-16. For figures 9, 11, 13, 14, and 15, multiple curves are shown within the same cell type. In these cases, the population of cells being plotted was divided into distinct subpopulations, such as cells that burst and cells that remained intact, in order to elucidate any perceivable differences in behavior. Figure 17 shows the % expansion of 3 different cell types over time.

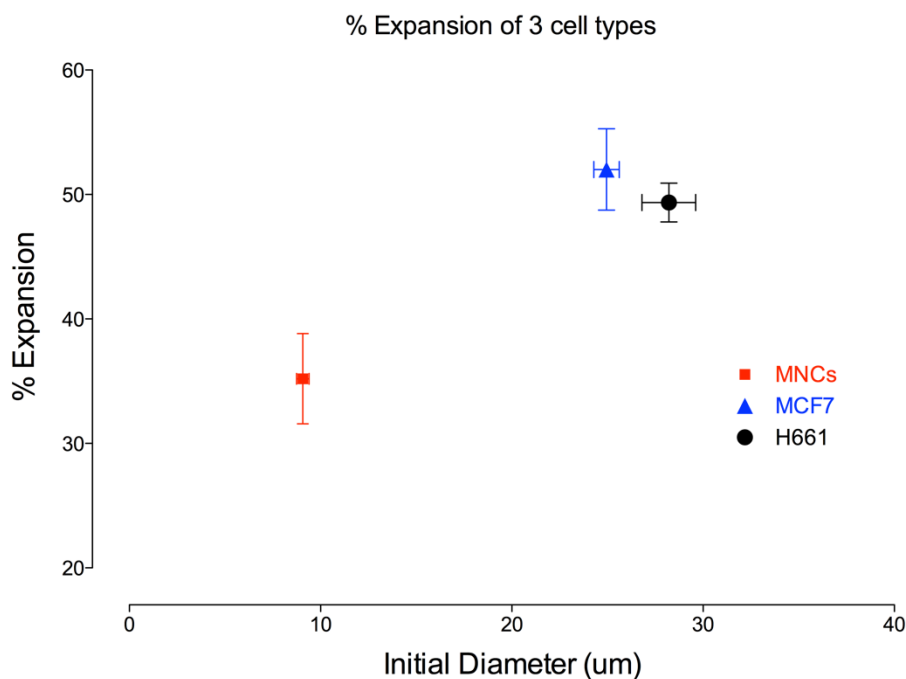


Figure 6. Percentage expansion of each of the 3 cell types studied, compared to the initial diameter. T-tests confirmed p-values <0.0001 , implying a significant difference in % expansion between each of the cell subpopulations. Also, there is no correlation found between % expansion and initial diameter.

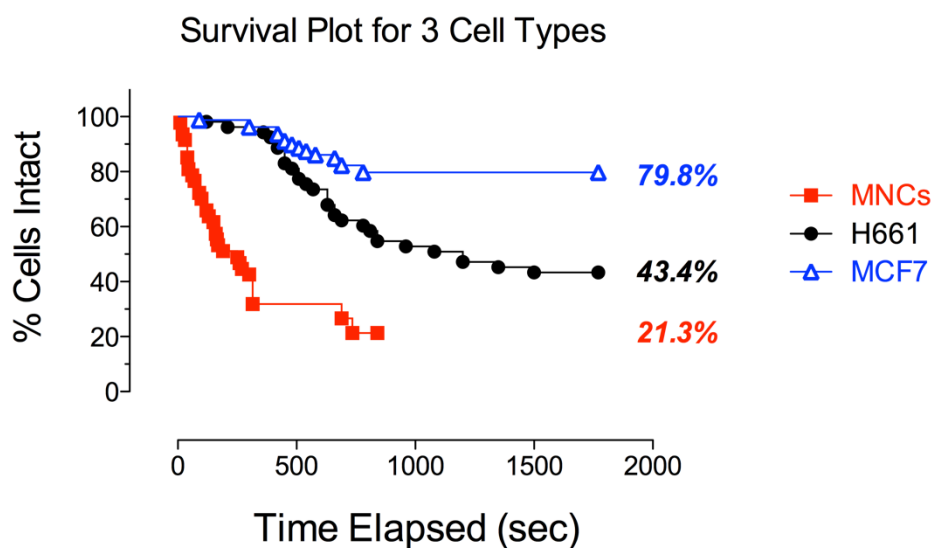


Figure 7. Survival plots for each of the 3 cell types tested. Also shown is the percentage of cells that remain intact by the end of the viewing period. Mantel-Cox Test yielded $p < 0.0001$ for all 3 comparisons, thus each cell type is significantly different from the others tested.

H661 Expansion Curves

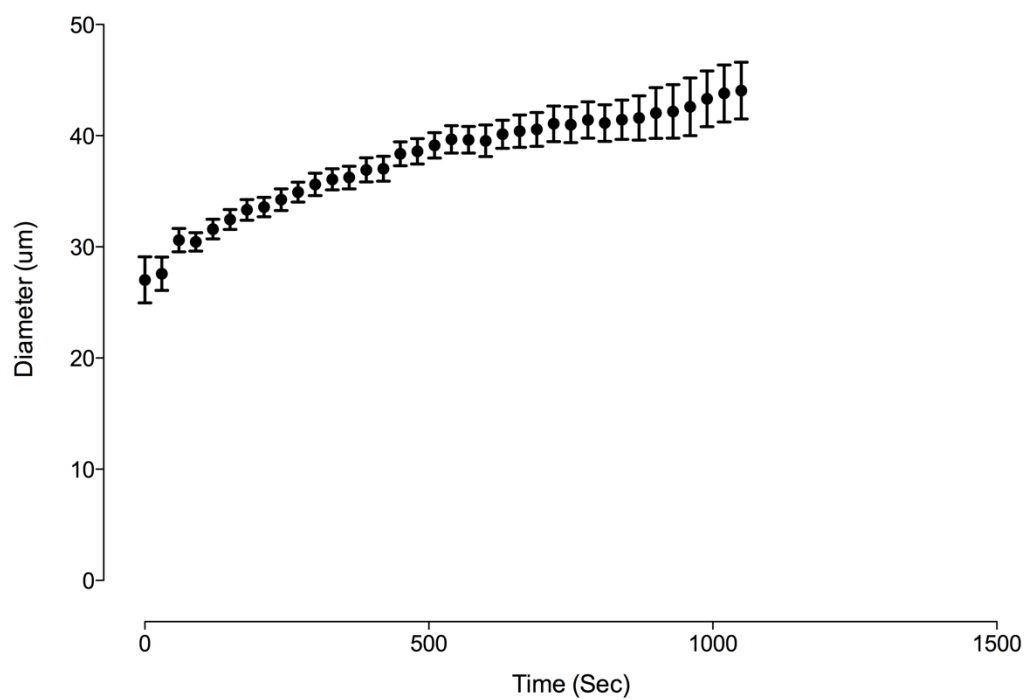


Figure 8. H661 expansion curve for all cells imaged, with diameter measured (μm) vs. time elapsed (sec). The mean of all diameters at each time point was plotted, $N=53$.

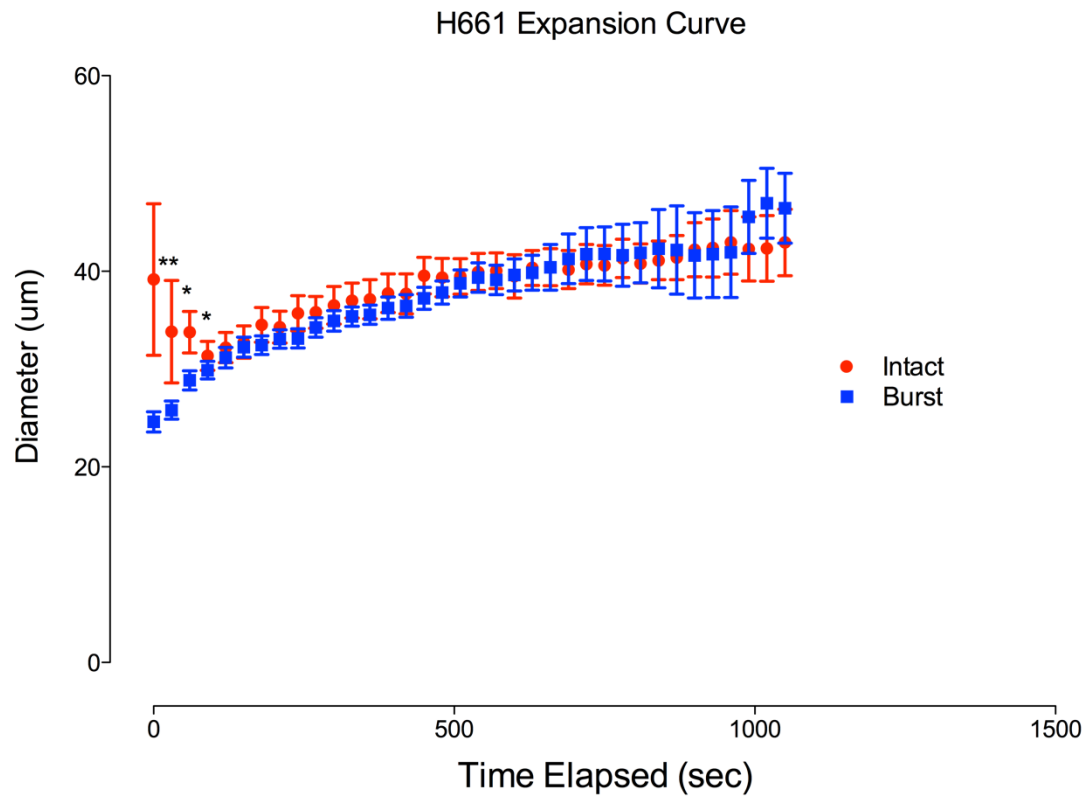


Figure 9. H661 Expansion curve of Diameter (μm) vs. Time (Sec). There are 2 plots, differentiating between cells that burst ($n=31$) and those that remain intact $n=22$). The data at the first 3 time points at $t = 0, 30$, and 60 seconds are significantly different (**: $p<0.01$, *: $p<0.05$). The mean of all diameters at each time point was plotted.

MCF7 Expansion Curves

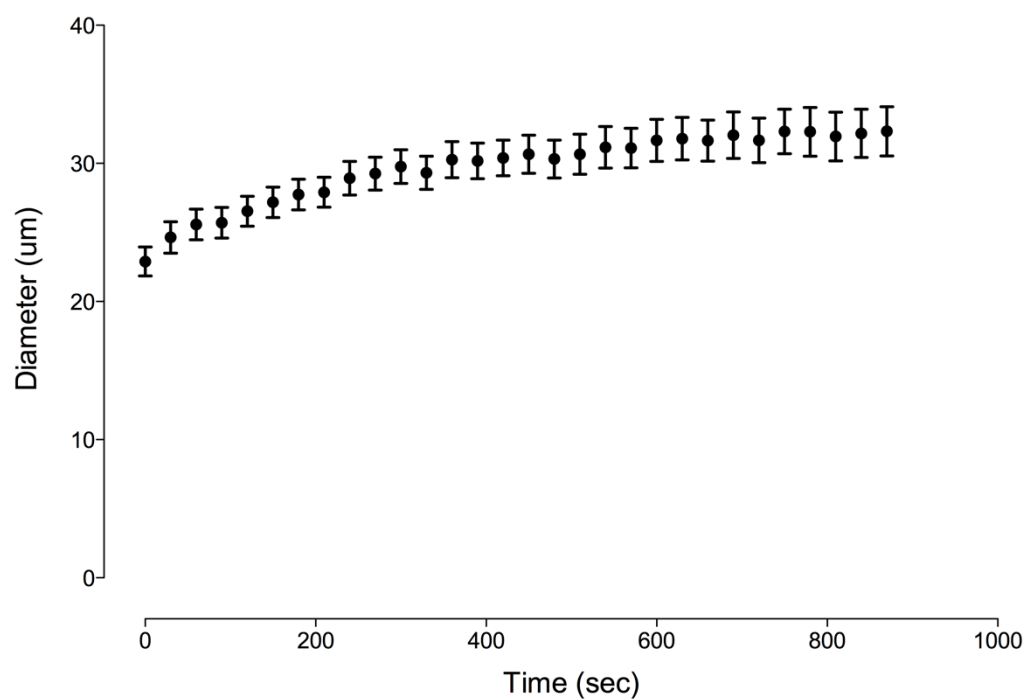


Figure 10. Representative MCF7 expansion curve for all cells imaged, Diameter (μm) vs. Time (sec). The mean of all diameters at each time point was plotted. ($n_{\text{total}} = 132$)

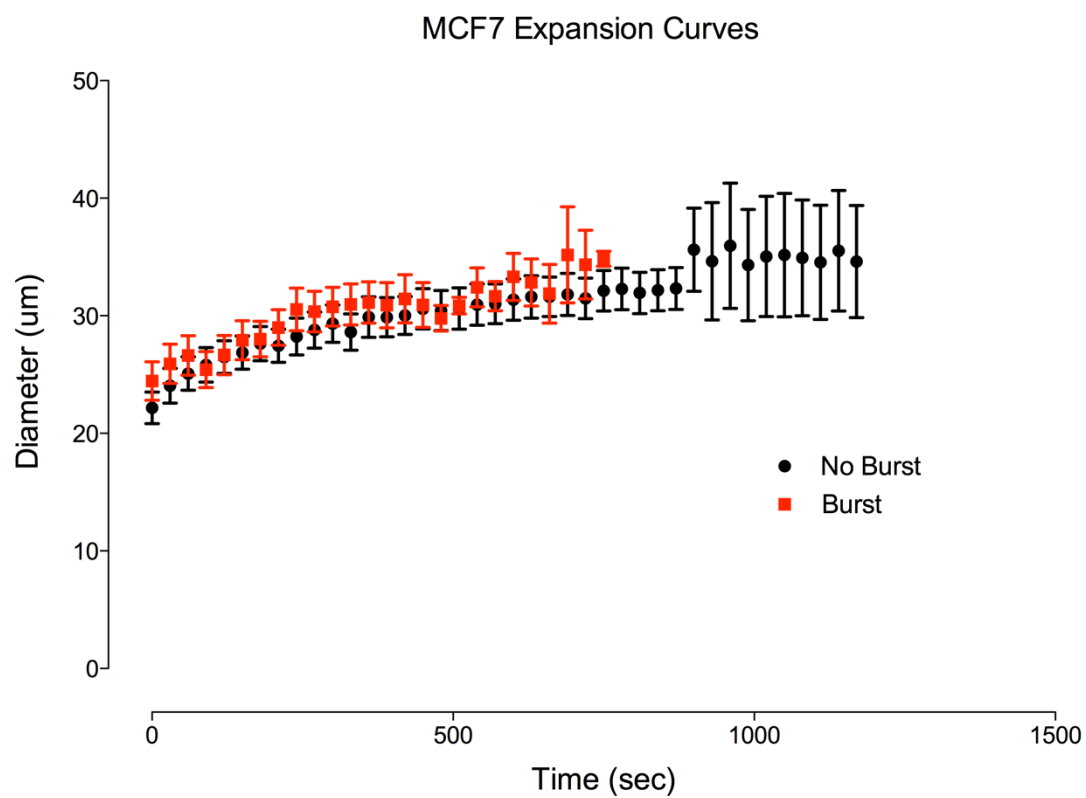


Figure 11. Representative MCF7 expansion curves of Diameter (μm) vs. Time (sec). There are 2 plots, differentiating cells that burst (n=13) and those that do not (n=28). The 2 subpopulations are not significantly different, with the minimum p-value of 0.6271 occurring at t = 690 seconds.

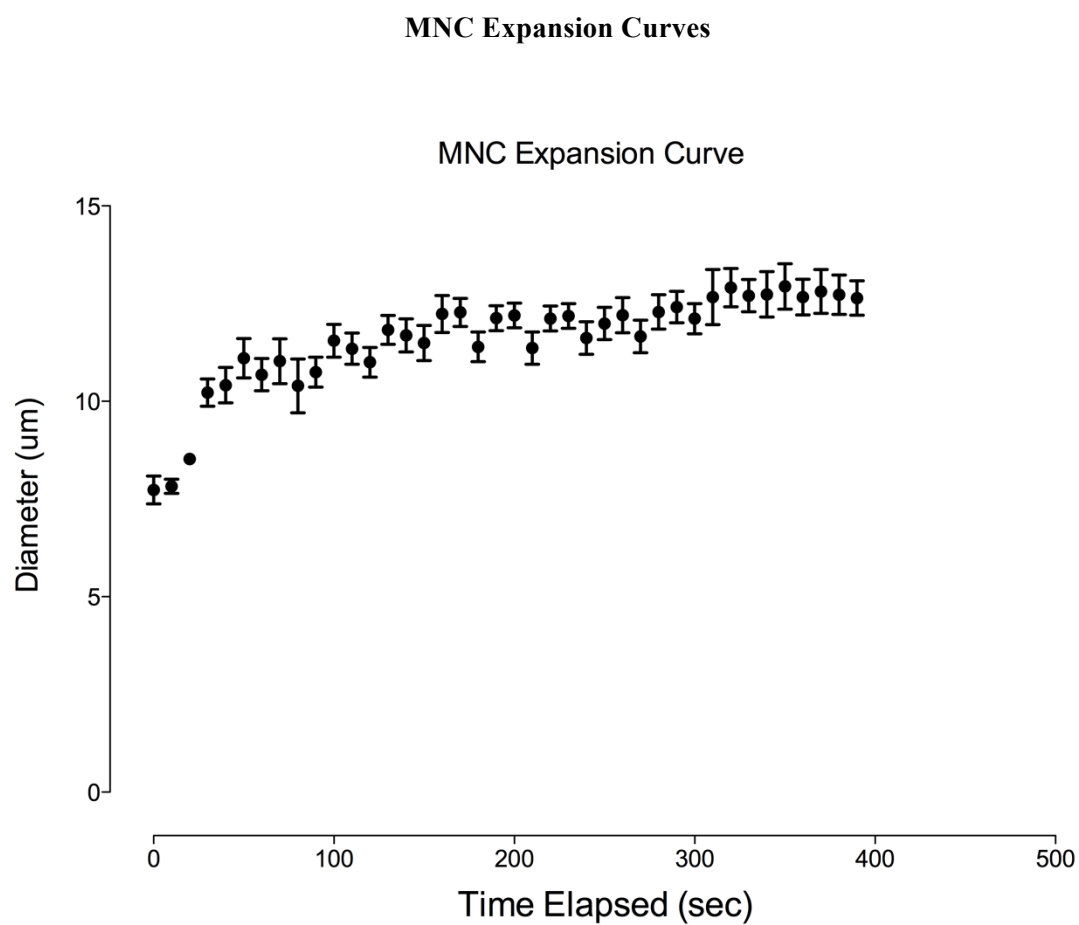


Figure 12. MNC expansion curve for all cells imaged, Diameter (μm). Vs. Time (sec). The mean of all diameters at each time point was plotted. (n=48)

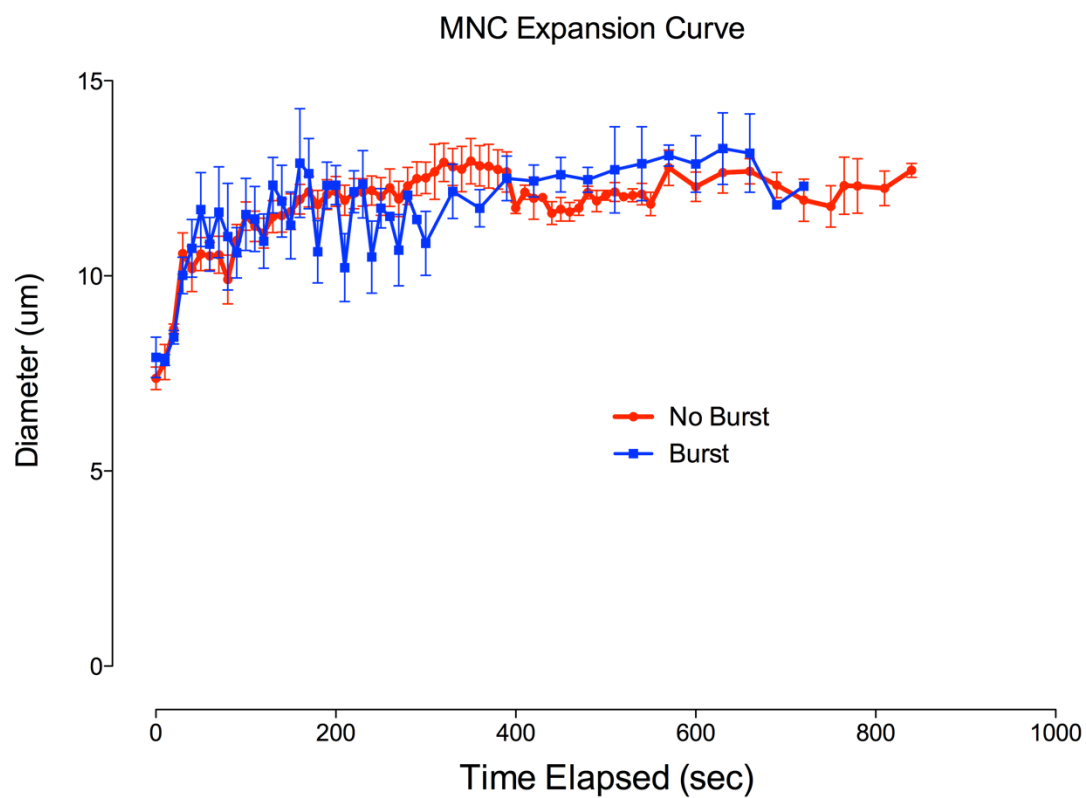


Figure 13. MNC Expansion curves of Diameter (μm) vs Time (sec). There are 2 plots for 2 cell subpopulations: those that burst ($n=31$) and those that remain intact ($n=17$).

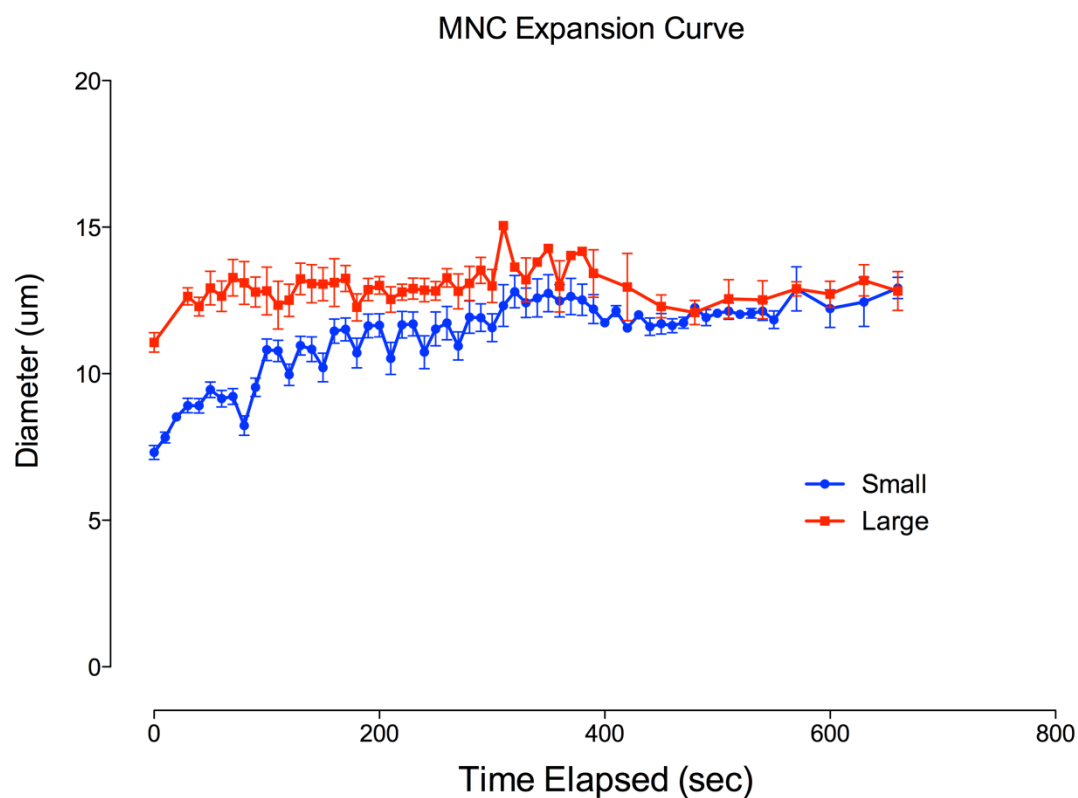


Figure 14. MNC expansion curves of Diameter (μm) vs. Time (Sec). Shown are 2 possibly distinct groups of cells, those with initial diameter larger than 10 μm , and those with initial diameter less than 10 μm . T-tests reveal a significant difference between the small ($n=33$) and large ($n=15$) data points, suggesting that the MNCs consisted of 2 subpopulations.

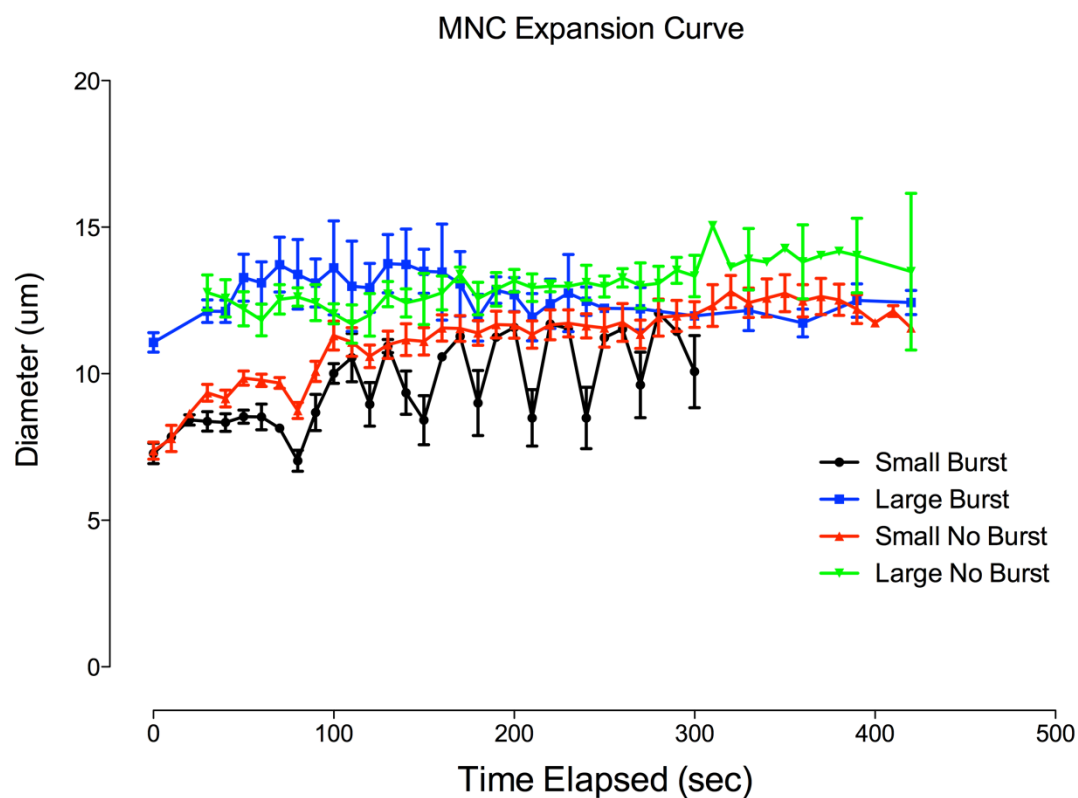


Figure 15. MNC expansion curves of Diameter (μm) vs. Time (Sec). The MNC cell population is divided into 4 distinct subgroups. Although some significant difference is seen, it is not enough to warrant dividing the MNC group into 4 subpopulations: 2 subpopulations of small and large are sufficient.

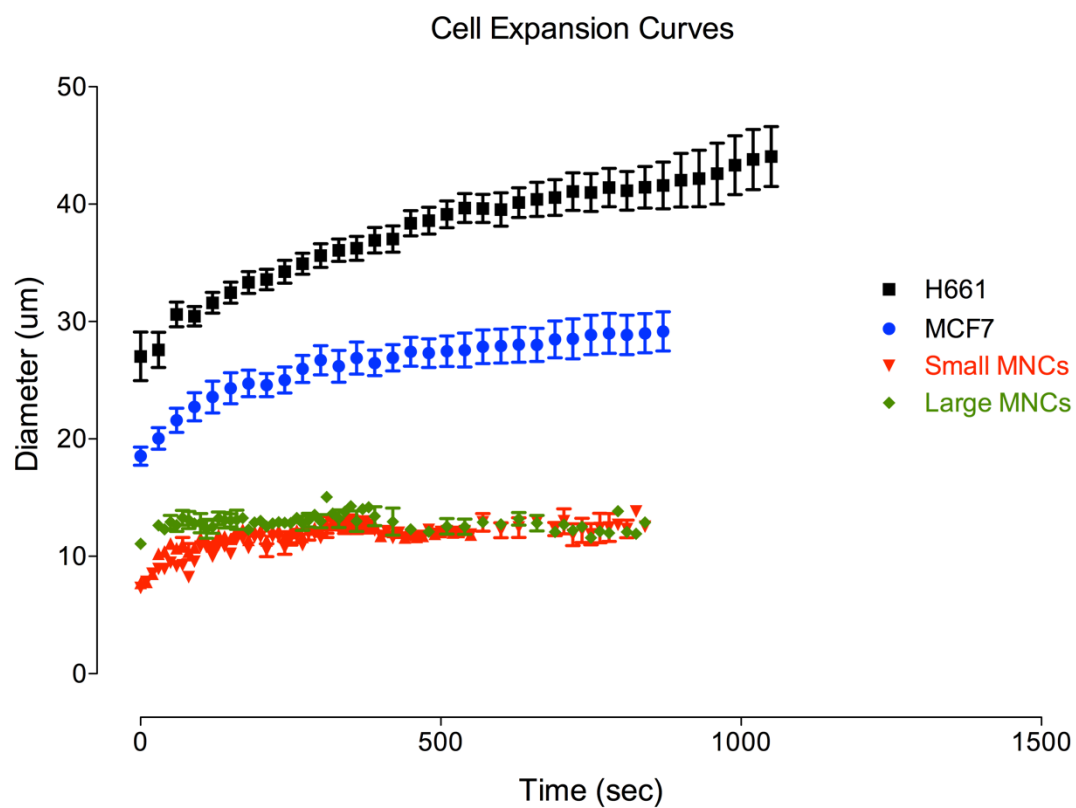


Figure 16. Representative expansion curves of Diameter (μm) vs. (Time (Sec) for each cell type plotted on same set of axes. Due to the statistical different between the 2 sets of MNC data shown in figure 14, the MNC data was divided into 2 subpopulations.

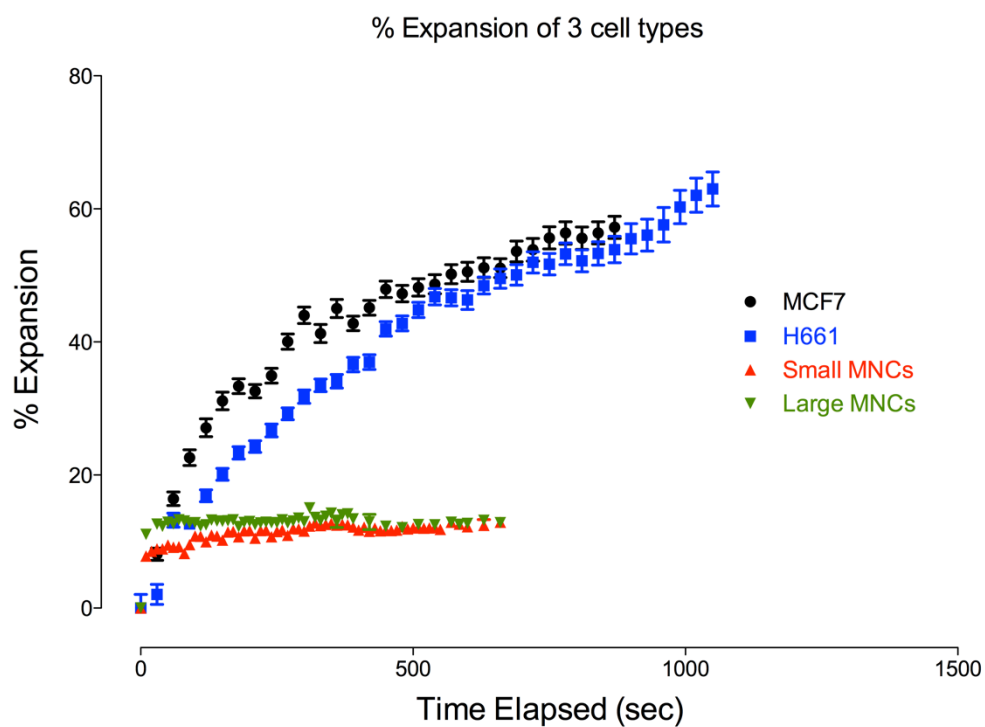


Figure 17. % expansion curve of MCF7, H661, small MNCs, and large MNCs. Expansion is measured relative to the mean cell diameter at time = 0 seconds, before being immersed in hypotonic solution.

Chapter 3

Analysis of Results

The dynamic curves showing the expansion behavior of the cells over time are distinct for each cell type. Figure 16 clearly contains 4 distinct expansion paths followed by different cell type. The MNC cell population has been divided into 2 subpopulations: small and large. Figure 14 shows the expansion behavior of these 2 subgroups, and how they are significantly different. T-tests on the data in figure 14 confirmed that the MNCs tested are likely a combination of 2 subpopulations. This is in agreement with theory, since MNCs can be a variety of white blood cells. Specifically, we predict the large MNCs to be monocytes, while the small MNCs are lymphocytes. The data shown in figure 16 was pooled from all the cells imaged of each cell type, regardless of whether they burst or not. Figures 9, 11, and 13 show no statistically significant difference between the data of burst cells or intact ones, hence we assume that the data can be pooled without causing any error or confusion.

In figure 17, % expansion of each cell type with respect to time is shown. The data sets are distinct, and yet follow a similar trend, they all increase to a certain % expansion exponentially before plateauing at that stage. We assume this stage to be the final diameter that the cells were able to be expanded to. Mechanical models were fit to this data, based on theory involving the membrane unfolding as well as an osmotic pressure gradient causing the cell to expand. The 2 models developed to fit this data are the ‘Kelvin-Voight Viscoelastic model’, and the ‘Osmotic Pressure Driving Force Model’.

Kelvin-Voight Viscoelastic Model

From a quantitative perspective, the expansion plots obtained for each cell type allows to effectively map the behavior of cell expansion in terms of a viscoelastic material. A Kelvin-Voight viscoelastic material (representative model shown in figure 18) behaves very much like the expansion plots. It is made up of a damping element and a spring in parallel. In this scenario, the membrane unfolding acts as a damper, since this is a time dependent action. The elastic component is due to the inherent elasticity in the plasma membrane. Thus, as a result of a constant stress applied, a plateauing exponential strain is observed before bursting at a max strain. The stress-strain equation of such a material is given by:

$$\sigma = E\epsilon + \eta \frac{d\epsilon}{dt}$$

$$\Rightarrow \epsilon(t) = \frac{\sigma_0}{E} (1 - e^{-\lambda t})$$

where $\lambda = \frac{E}{\eta}$

Figures 19-23 show viscoelastic model curves fit to the expansion data for each cell type.

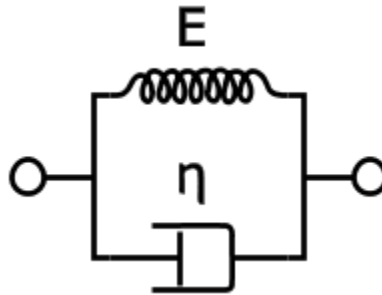


Figure 18. Kelvin-Voight viscoelastic material model. The model consists of an elastic spring and a linear damping element placed in parallel.

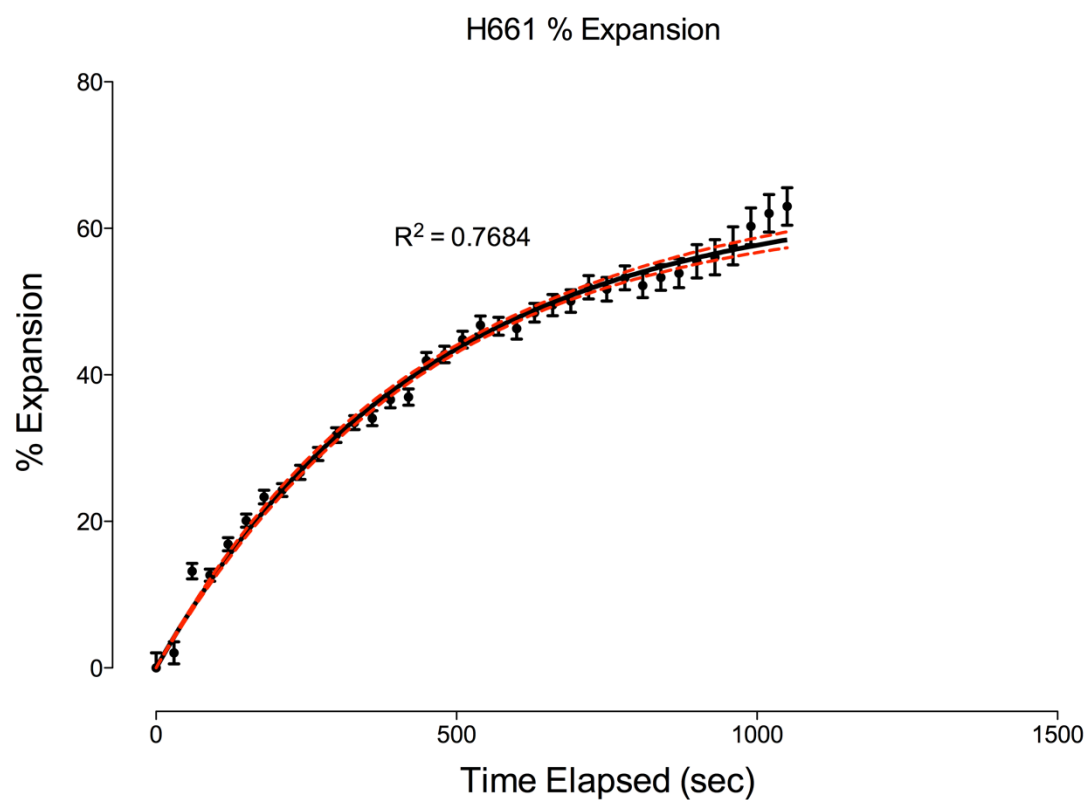


Figure 19. H661 % Expansion plot with viscoelastic model curve fit. The dashed red lines represent a 95% confidence interval in the curve fit.

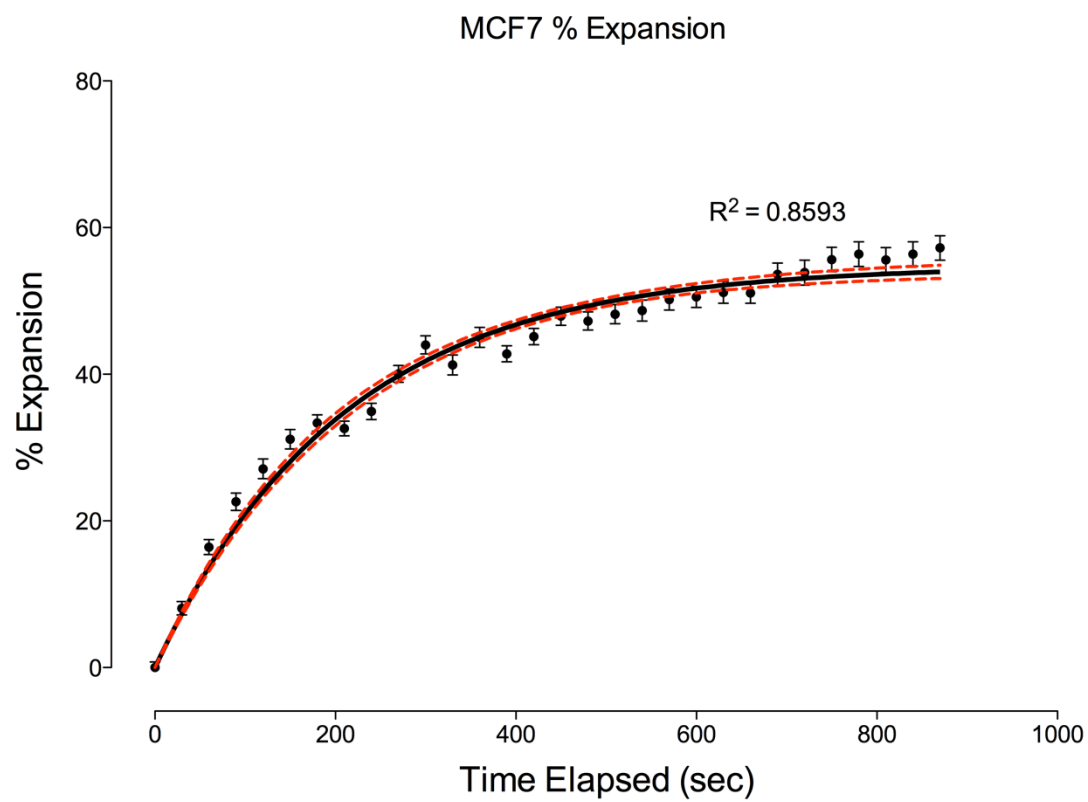


Figure 20. MCF7 % Expansion with viscoelastic model curve fit. The dashed red lines represent a 95% confidence interval in the curve fit.

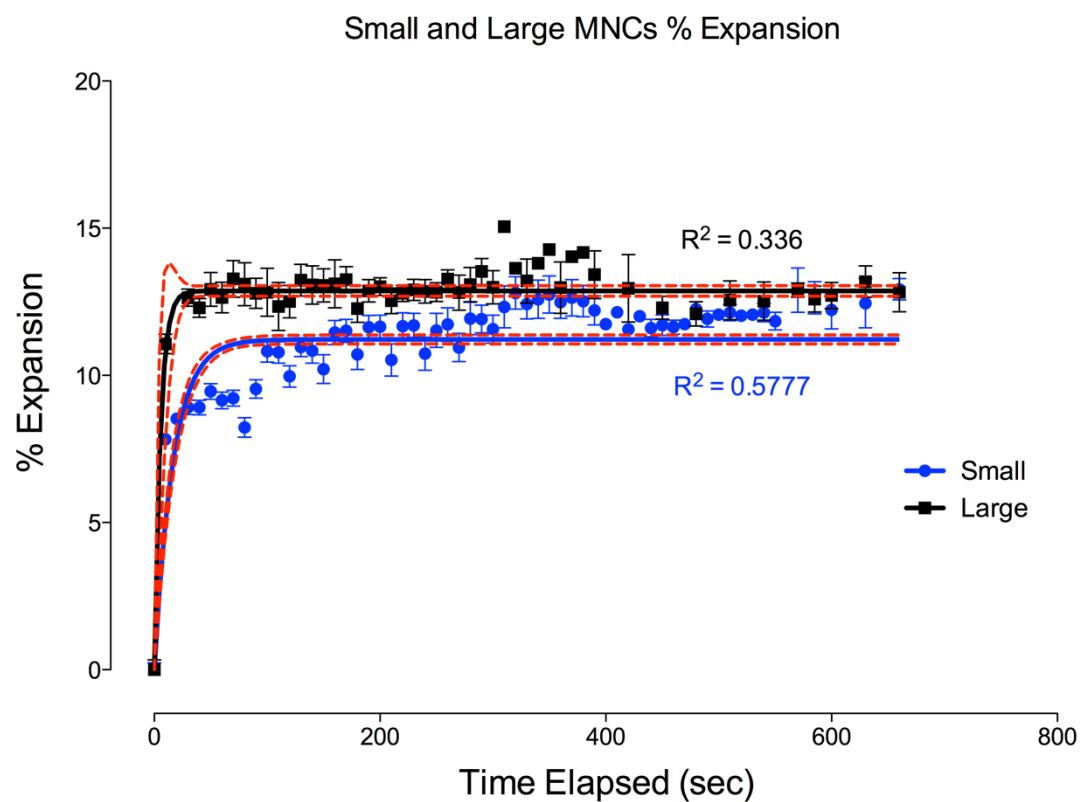


Figure 21. Small and large MNCs % expansion with viscoelastic model curve fit to each. The dashed red lines represent a 95% confidence interval in the curve fits.

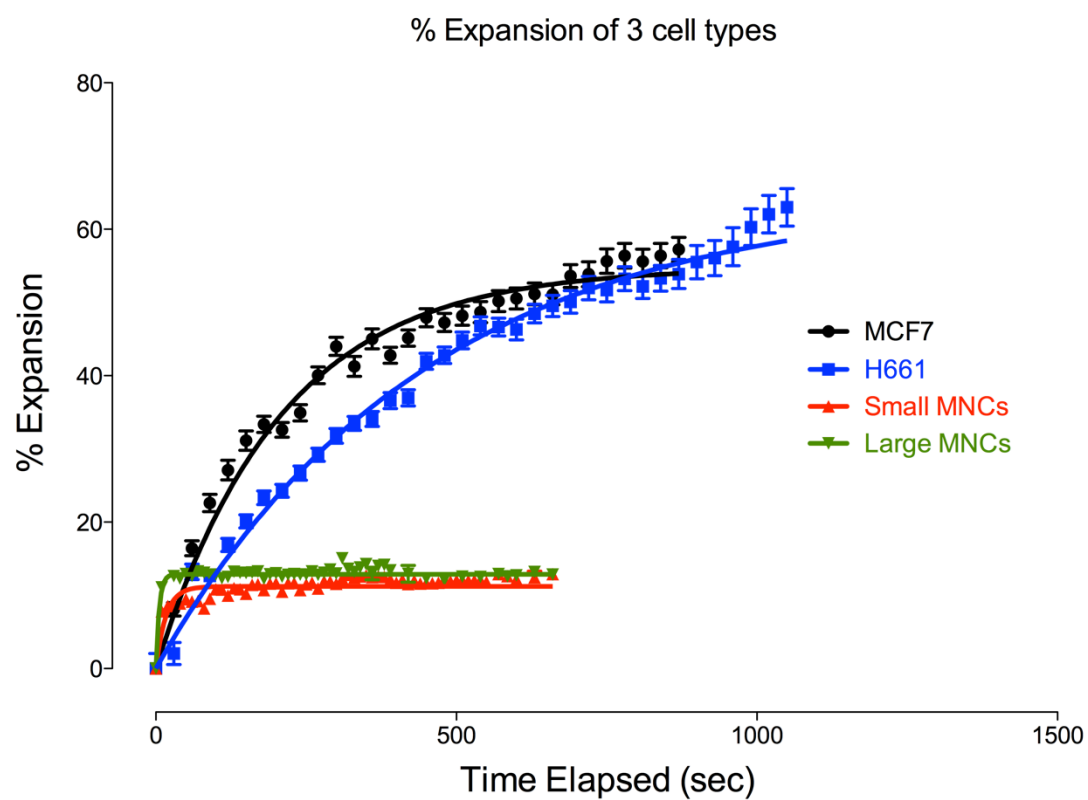


Figure 22. Comparison of % expansion of MCF7, H661, Small MNCs, and Large MNCs. Also shown are the curve fits for each data set according to a viscoelastic model.

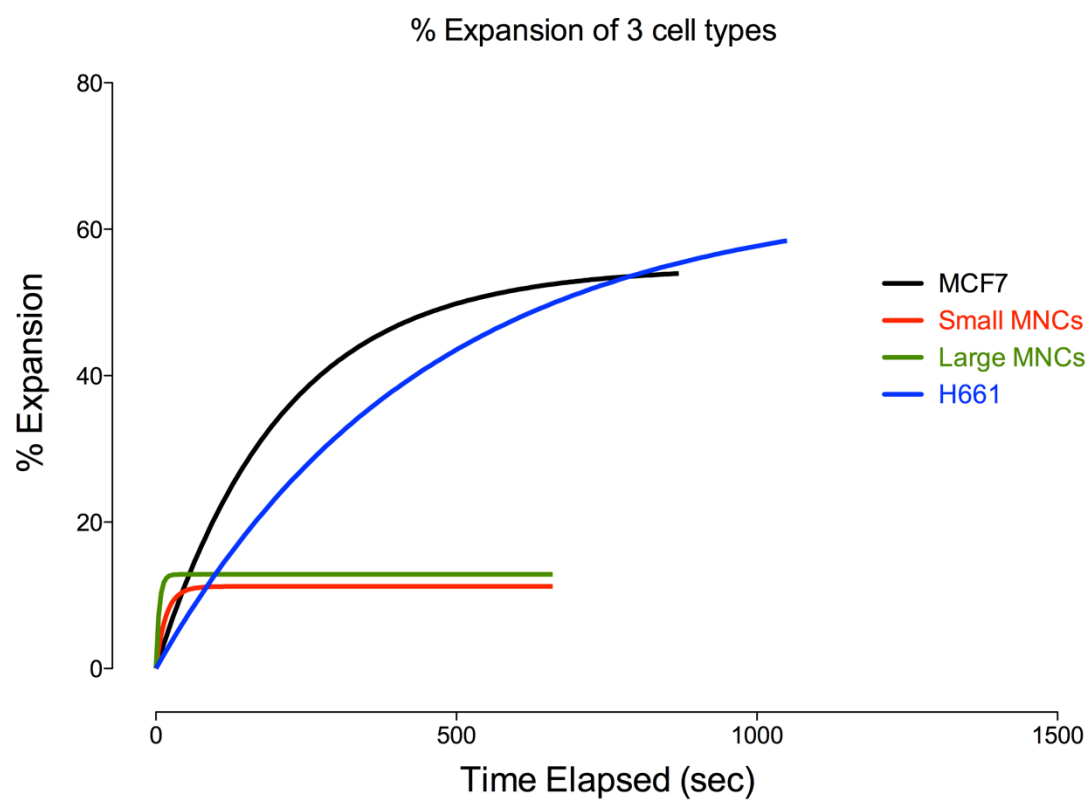


Figure 23. Viscoelastic curve fits for MCF7, H661, Small MNCs, and Large MNCs.

The curves shown in figures 19-23 all have the equation shown below. The values of the constants of each curve are shown in table 1.

$$\% \text{ Expansion} = C[1 - e^{-kt}]$$

where $C = \frac{\sigma_o}{E}$ and $k = \frac{E}{\eta}$

Table 1. Table showing values of constants for viscoelastic model curve fits.

Cell type	C	k	R²
<i>MCF7</i>	54.8	0.004801	0.8593
<i>H661</i>	64.54	0.002245	0.7684
<i>Small MNCs</i>	11.22	0.06025	0.5777
<i>Large MNCs</i>	12.87	0.1840	0.3336

Osmotic Pressure Driving Force Model

Cell expansion can also be modeled by considering the osmotic pressure gradient created by placing the cell in a hypotonic solution. Specifically, we let the determining factor causing the expansion to be the flux, Q , of water into the cell.

$$Q = \frac{dV}{dt} = K_1 * (P_{out} - P_{in}) = k_1 \Delta P$$

Where K_1 is the permeability of the membrane to water molecules, and P_{out} and P_{in} are the osmotic pressures outside and inside the cell, respectively. We assume K_1 to be constant throughout the expansion process.

But:

$$\Delta P \propto \Delta C$$

Where C is the concentration, given by:

$$C = \frac{\text{Solutes}}{\text{Volume}} = \frac{S}{V}$$

Therefore,

$$\frac{dV}{dt} = k_1 \Delta P = k_1 k_2 \Delta C = k_1 k_2 \left(\frac{S}{V} \right)$$

Where k_2 is the constant of proportionality between ΔP and ΔC .

Integrating from the initial volume V_o at time 0 to an arbitrary time, t :

$$\int_{V_o}^V V dV = \int_0^t k dt$$

Which simplifies to:

$$\frac{V^2}{2} - \frac{V_o^2}{2} = kt$$

$$\Rightarrow V^2 - V_o^2 = 2kt$$

Recognizing that V is the volume of a sphere and is given by:

$$V = \frac{4}{3}\pi R^3 = \frac{\pi D^3}{6}$$

Where R and D are the radius and diameter of a sphere, respectively.

Then:

$$\left(\frac{\pi}{6}\right)^2 (D^6 - D_o^6) = 2kt$$

Where D_o is the initial diameter of the cell.

After some manipulation, we obtain an expression for D as a function of time:

$$D = \sqrt[6]{Bt + D_o^6}$$

Where B is a combined constant and D_o is the initial diameter of the cell.

To derive a strain equation from this we use the definition of strain, ϵ :

$$\epsilon = \frac{D - D_o}{D_o} = \sqrt[6]{\frac{Bt}{D_o^6} + 1} - 1 = \sqrt[6]{Kt + 1} - 1$$

Where the constant $K = \frac{B}{D_o^6}$

In addition to the strain inducing pressure force created inside the cell due to fluid flux, there is a restoring elastic force proportional to the radius of the cell, acting in a manner against expansion. This is in accordance with the Law of Laplace, which dictates that the tension in the wall of a spherical or cylindrical pressure chamber is proportional to the chamber's radius. Thus, we can model the cell as a sphere, and represent the force as having an effect

$$\frac{dD}{dt} = -ER = \frac{E}{2}D$$

Where R and D are the radius and diameter of the cell.

Integrating:

$$\ln D = -\frac{E}{2}t + C$$

Therefore,

$$D = C_2 e^{-E_2 t}$$

However, since the force is a restoring force, we add a minus sign to the diameter function in terms of time, to obtain:

$$D = -C_2 e^{-E_2 t}$$

Similar to above, deriving strain from the above equation:

$$\epsilon = -K e^{-E_2 t} - 1$$

Finally, combining the 2 equations for strains, the total strain is given by:

$$\epsilon_{tot} = \sqrt[6]{K_1 t + 1} - K_2 e^{-E_2 t} - 2$$

Figures 24-28 show the expansion plots for MCF7, H661, Small MNCs, and Large MNCs with curves fitted to the nonlinear strain model derived above. Note that strain is identical to %

expansion divided by a factor of 100. Thus, the constants K_1 and K_2 will be a factor of 100 larger in the % expansion curve fits.

It is important to note that the final strain function derived above is meaningless for negative times. In fact, a point of discontinuity is reached when $t = -1/K_1$. For the purpose of fitting this to expansion data, we only consider the portion of the function from time $t = 0$ sec to the final time measured, or the time of bursting in some cases.

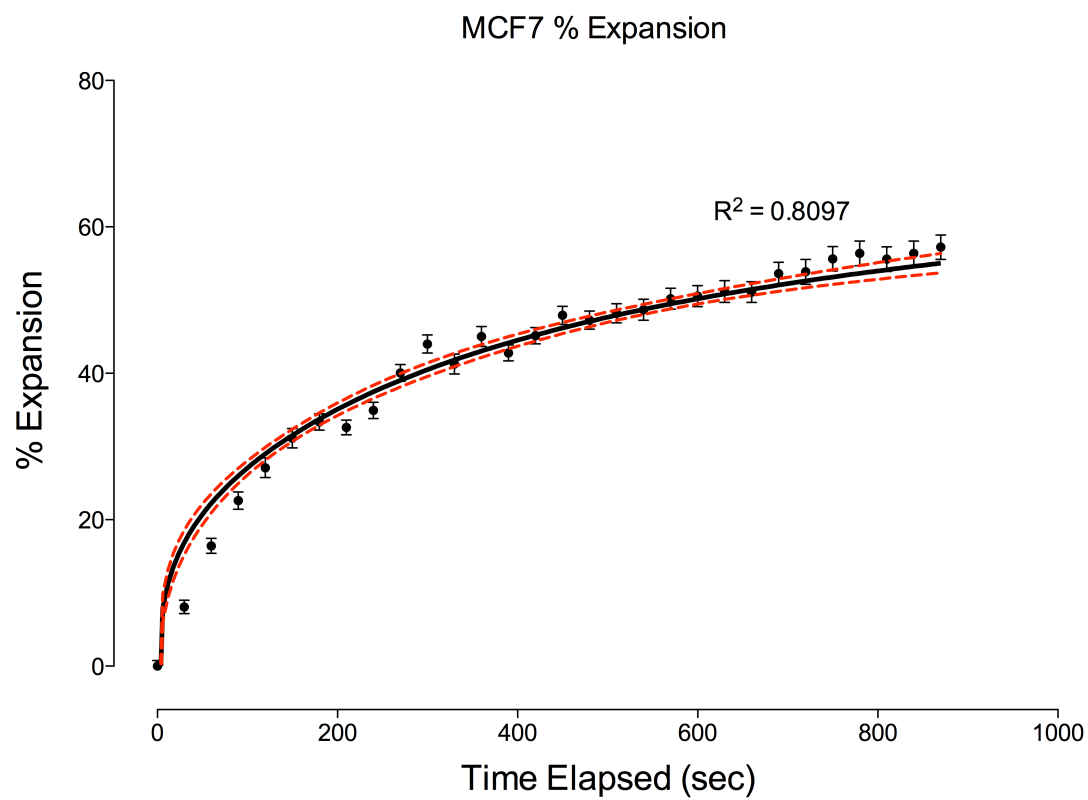


Figure 24. MCF7 % Expansion with osmotic pressure driving force model curve fit. The dashed red lines represent a 95% confidence interval in the curve fit.

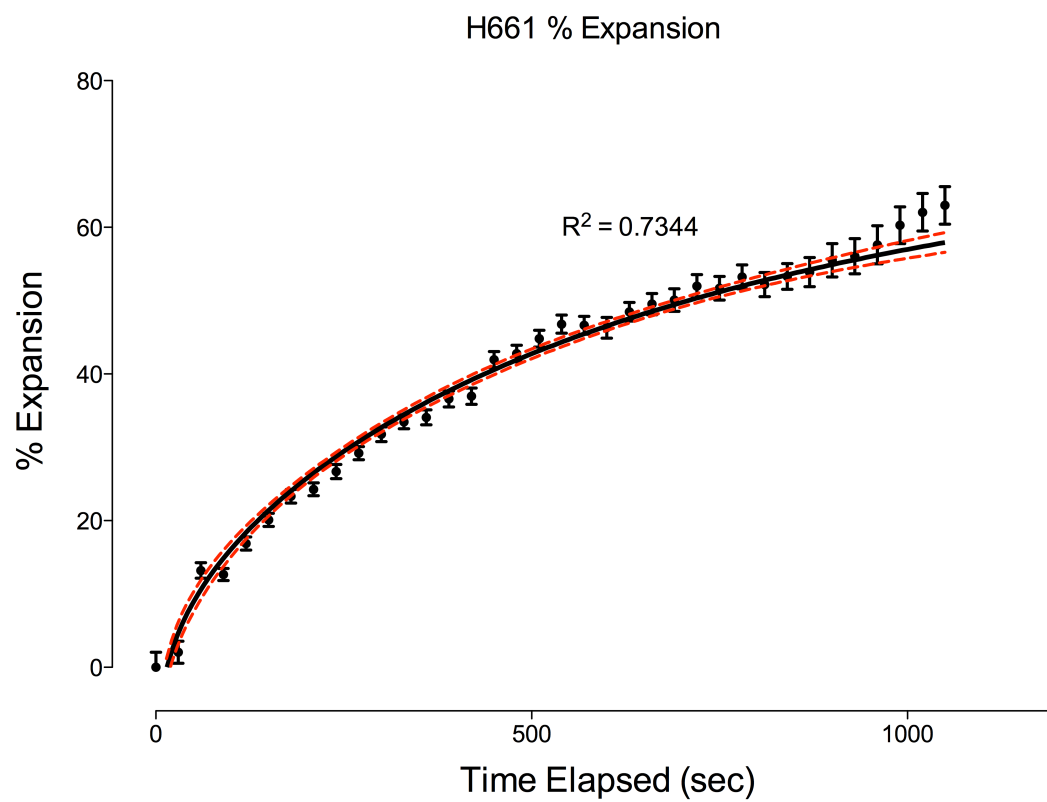


Figure 25. H661 % Expansion with osmotic pressure driving force model curve fit. The dashed red lines represent a 95% confidence interval in the curve fit.

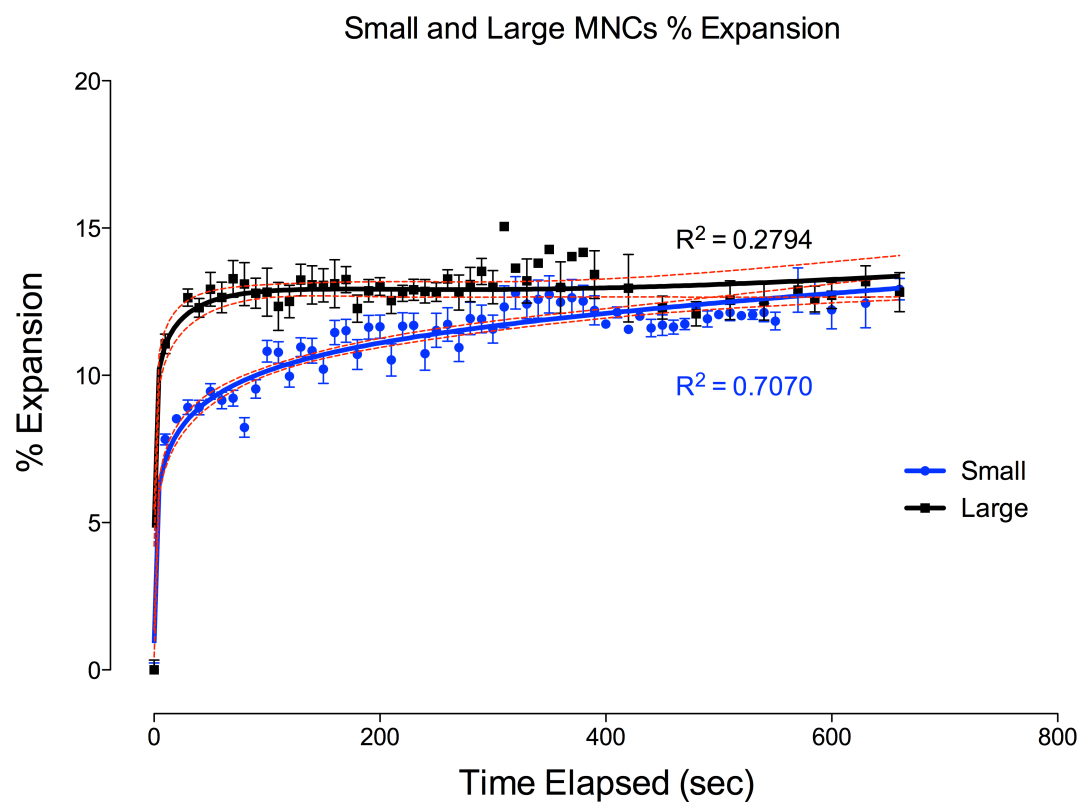


Figure 26. Small and Large MNCs % Expansion with osmotic pressure driving force model curve fits for each. The dashed red lines represent a 95% confidence interval in the curve fits.

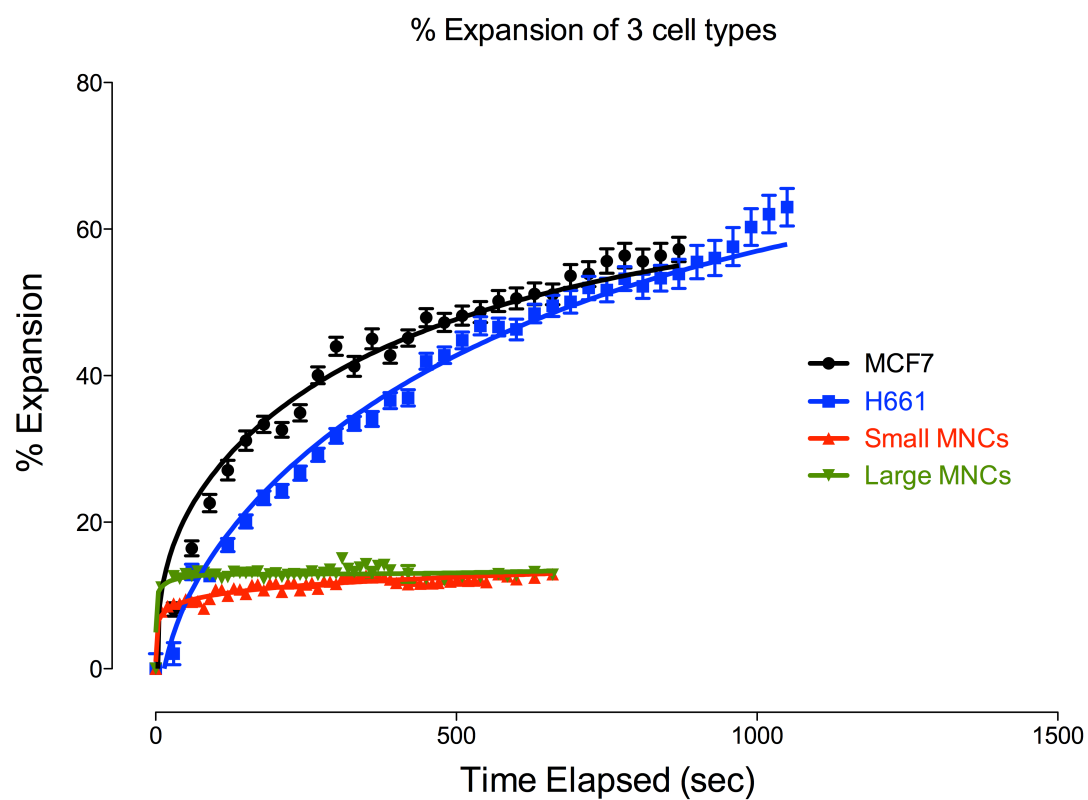


Figure 27. % Expansion of MCF7, H661, Small MNCs, and Large MNCs. Also shown are the osmotic pressure driving force model curve fits to each.

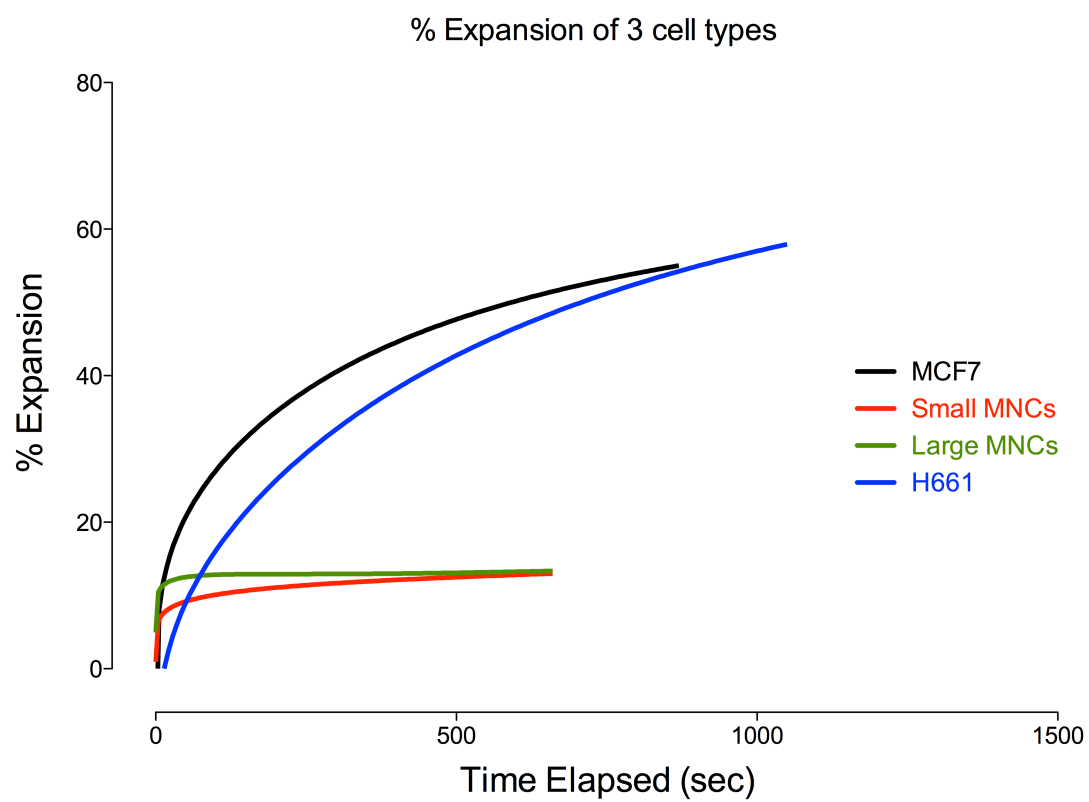


Figure 28. MCF7, H661, Small MNCs, and Large MNCs osmotic pressure driving force model curve fits.

The exact values of the constants K_1 , K_2 , and E_2 for each curve fit drawn for the osmotic pressure driving force model are shown in table 2. Shown below is the equation to be fitted by each curve.

$$\% \text{ Expansion} = \sqrt[6]{K_1 t + 1} - K_2 e^{-E_2 t} - 2$$

Table 2. Values for constants in the total strain equation for the osmotic pressure driving force model. The values reflect the equation of the curve fit plotted to each set of data.

Cell Type	K_1	K_2	E_2	R^2
<i>MCF7</i>	4.415e7	15.59	0.003106	0.8097
<i>H661</i>	6.711e7	30.49	0.001858	0.7344
<i>Small MNCs</i>	15118	-1.910	0.002866	0.7070
<i>Large MNCs</i>	16604	-5.832	0.003831	0.2794

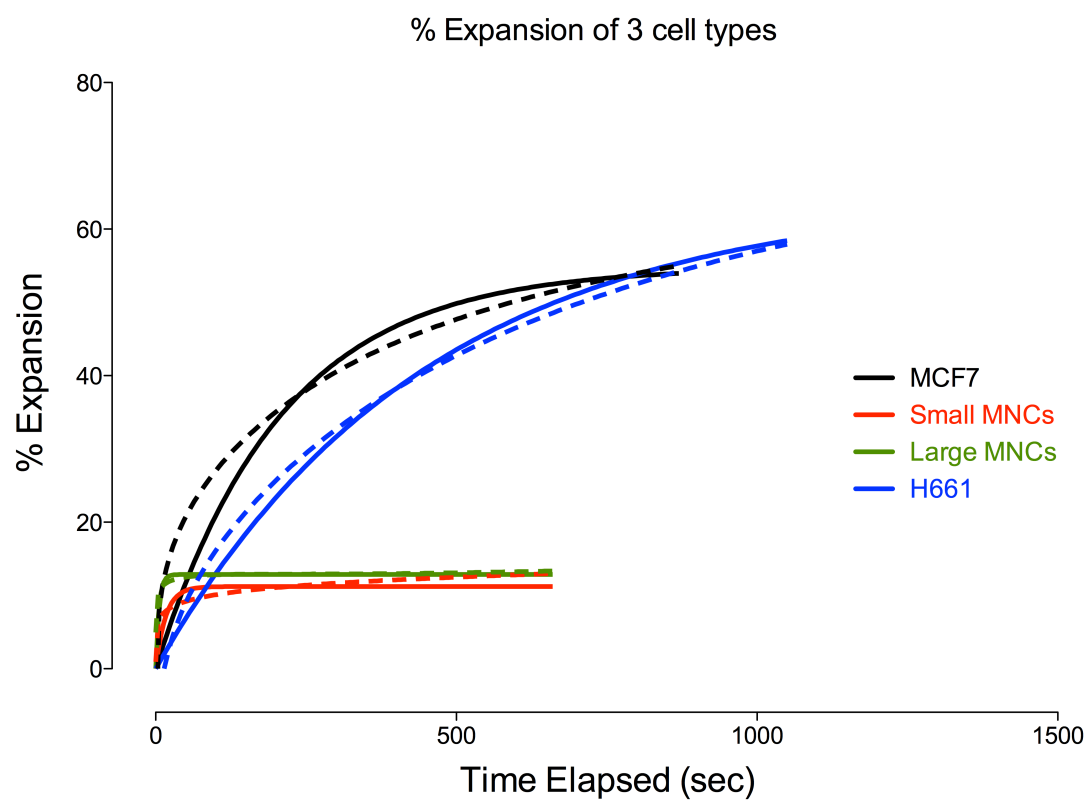


Figure 29. Viscoelastic model (solid curves) and osmotic pressure driving force model (dashed curves) curve fits for MCF7, H661, Small MNCs, and Large MNCs.

Chapter 4

Discussion

The results collectively support the principal initial hypothesis that mononuclear peripheral cells exhibit distinct mechanical characteristics than cancer cells. It is primarily on this basis that mechanical CTC separation from blood can occur effectively and reliably. These mechanical characteristics are 3 fold: (1) is the maximum % expansion undergone by each cell type, (2) is the % of intact cells at the conclusion of imaging, and (3) is the dynamics of the expansion process.

The end-point analysis plotted in figure 6 shows a distinct difference in the initial diameter as well as the percentage expansion undergone by the different cell populations. Statistical T-tests confirmed a significant difference between each of the 3 cell populations ($p < 0.0001$). Figure 6 also shows that there is no correlation between initial diameter and % expansion when comparing multiple cell populations. The extent of expansion undergone by the cancer cells is significantly high, much higher than the 10% elastic expansion achievable by stretching the plasma membrane. Thus, a 50% expansion of a cell necessitates some sort of mechanism to complement the membrane stretching. We hypothesize that the extra membrane available for expansion is initially present as folds, and only unfolds when necessary. The 2 figures in Appendix B, showing a timeline of H661 and MCF7 expansions support this hypothesis. Specifically, the H661 cells expanding appear to go through an ‘unfurling’ stage, when the membrane is uneven and full of wrinkles. The wrinkles then even out and the cell becomes round again before bursting. The MCF7 cell expansion timeline shown in Appendix B displays a similar yet different behavior. Rather than a large scale unfurling of the membrane, a bleb forms. Blebs are caused by a separation of the membrane from the cytoskeleton, making it

easier for it to expand (Charras & Paruch, 2008). Since blebs detach from the cytoskeleton they might better reflect the true extent to which a membrane can expand. Although the increased diameter of the cell evens out over time as the cell becomes spherical again, it is possible that a stress concentration is created in the section of the membrane where the bleb developed, due to over-expanding of this section compared to other plasma membrane sections. It could also be that the bleb is the first instance of membrane detachment from the cytoskeleton, and that as the cell continues to expand, the rest of the plasma membrane also detaches from the cytoskeleton. The models developed here for cell expansion assume a uniform expansion of the membranes at all times, but it is worth mentioning the bleb phenomenon that occurs in some cases of cell expansion. Blebs have been shown to occur in apoptosis, cytokinesis, and tumor cell extravasation. The fact that some cells placed in hypotonic solutions expand through blebbing might suggest a number of behaviors. It might be a sign of apoptosis, due to the extreme stress the cell is under. However, it could also be a sign of adaptation, in that the cell is allowing itself to swell to accommodate for osmosis, and possibly avoid bursting.

The survival plot shown in figure 7 also illustrates a clear difference in the behavior of each cell population when exposed to hypotonic stress. As expected, the majority of MNCs burst (79%) fairly rapidly after exposing to hypotonic shock. However, each cancer cell type followed a unique behavioral trend, with the MCF7 cells being substantially more resilient to bursting (21.2% burst) than the H661 cells (56.6% burst).

For all the analyses conducted here, the data from each cell population was pooled, regardless if the cell in question eventually burst or not. Figures 9, 11, and 13 investigate whether this assumption is justified. Statistical t-tests confirmed that the behavior of cells that eventually burst vs. intact cells belonging to MCF7 and MNC populations were not significantly different. For H661, the diameter in the first 90 seconds differed significantly between cells that eventually burst and those that remain intact. This is shown in figure 9. However, considering the relatively

small time frame where this difference is significant, it was decided to consider the 2 populations of cells that eventually burst and cells that remain intact as a single joint population behaving in similar fashions.

When examining MNC subpopulations, it was found that the cells could be divided into small and large cells. Small cells had initial diameter less than 10 μ m, while large cells had initial diameter larger than 10 μ m. This separation of MNC data yielded 2 significantly different subpopulations in terms of expansion behavior, as shown in figure 14. Ironically, this was reassuring, as it addressed one of the concerns with using Ficoll as a means to isolate white blood cells. Ficoll centrifugation of blood yields a thin layer of mononuclear white blood cells containing multiple cell types. We predict that the cells in the ‘Large MNC’ subpopulation are monocytes and that cells in the ‘Small MNC’ subpopulation are lymphocytes. While both monocytes and lymphocytes are important to consider in designing blood CTC isolating mechanisms, it is also important to examine the mechanics of neutrophils. Neutrophils are the immune cells primarily responsible for phagocytosis in the body, and are thus likely to have the most expansion capabilities among white blood cells.

Figure 16 shows the diameter vs. time expansion plots for MCF7, H661, and MNCs. It is evident here that, not only are the cancer cells expansion plots distinct from the MNC plots, but that cancer cells each follow distinct expansion curves. Examining figure 17, the % expansion plots of tumor cells resemble each other more than when plotting absolute diameter expansion plots, although statistical t-tests reveal that they remain significantly different. The distinctness among cancer cells in their percentage final expansion, survival rate, and expansion dynamics raises the possibility of determining cancer phenotype by looking at the mechanical properties rather than on the biological and chemical factors expressed. Replicating the experiments performed here on other cancer cell lines would yield additional data that could support this possibility.

Two models, each focusing on different aspects of cell expansion were constructed to attempt to fit the data obtained for each cell population. The first focused purely on modeling the membrane behaving effectively as a viscoelastic material. A Kelvin-Voight model was chosen, consisting of an elastic element and a damping element in parallel with each other. In context, the membrane elasticity acts in conjunction with the membrane unfolding, with the unfolding acting as the damper in the expansion process. The applied stress is assumed to be a step input at time $t=0$ seconds, and is constant over the course of the experiment. Results of this model (figures 19-23) fit fairly well to the MCF7 and H661 data (R-square 0.8593 and 0.7684, respectively), but were relatively poor fits to both small and large MNC data (R-square 0.5777 and 0.336, respectively). We can nevertheless make important observations as to the differences in mechanical properties among the cells using the values of equation constants shown in table 1. As expected, the MNCs have the lowest C values, which correspond to the highest elastic modulus. A higher elastic modulus implies a smaller deformation for a given force. Thus, the MNCs expand substantially less than the cancer cells. Among the cancer cells, MCF7 was stiffer than H661, with a lower C value. This agrees with the survival and end-point data showing MCF7 as being stiffer cells, more resistant to both deformation and bursting. Also, MNC fits had k values an order of magnitude larger than the tumor cells. The k-parameter is equal to the elastic modulus divided by the damping coefficient. From an order of magnitude analysis, we can conclude that the damping coefficient variation between the cell populations is the primary cause for the substantial difference in k values. Specifically, MNCs have much smaller damping coefficients than H661 and MCF7 cells, while the cancer cells both had similar damping coefficients. In other words, the MNCs have much less membrane to unfold and so have smaller damping coefficients.

The problem with the MNC fit (and to a certain extent, the H661 fit) was the plateauing effect that the viscoelastic model predicted. The MCF7 data fit the best as they were the most resistant cells to bursting, and thus their surface area expanded much more reluctantly, and only

to a certain maximum. The H661 on the other hand, continued to expand gradually, even after long time periods. We predict that this also caused the poor MNC fits. Another cause of poor MNC fits is likely due to the higher degree of variability in the MNC data. A relatively small number of MNCs imaged ($n=32$) might have contributed to a rougher curve, compared with the tumor cell data. Also, since MNC initial diameter and % expansion is substantially less than that of the tumor cells, it increases the impact of any error and uncertainty during the image processing stage. Whether the images were analyzed using MATLAB scripts, or ImageJ, both introduce uncertainties. MATLAB image processing inevitably involves applying filters and transforms to the original image, while manual ImageJ analysis is limited by the human eye and picture resolution.

The second model fit to the data focused on the osmotic pressure gradient created when placing the cells in a hypotonic solution. In essence, the driving force for expansion decays over time, as the solution concentrations inside and outside the cell become more and more similar due to osmosis. Simultaneously, there is a restoring elastic force that becomes more significant as the cell expands, eventually overtaking the decaying osmotic force. The mathematical function reflective of this model was only valid up to the maximum point where the % expansion peaks. Notwithstanding this limitation, it nevertheless was able to fit the expansion plots reasonably well.

R-square values for the osmotic pressure gradient curve fit for MCF7 and H661 cells were 0.8097 and 0.7344 respectively, similar to those generated by the fits according to the viscoelastic model previously discussed. The curve fit to the large MNC data was poor with an R-square value of 0.2794. However, the fit to the small MNC data was substantially improved over the viscoelastic model ($R\text{-square} = 0.7070$). Practically, these results suggest that this model lends itself more readily to a wider variety of cell expansions than does the viscoelastic model.

However, as previously mentioned, the uncertainty and variation in the MNC data necessitate further investigation before an affirmative case for either model can be made.

Several aspects of cell mechanics could be incorporated into each model to improve them. The viscoelastic model could incorporate the action of cytoskeletal filaments such as actin and keratin in impeding or helping cell expansion. It would also have to consider what effects hypotonic stress has on these filaments, and whether or not it renders them inactive. The osmotic pressure model could be improved by making the permeability of the cell membrane to water variable with time. Water can enter a cell through 2 mechanisms: diffusion through the phospholipid bilayer, and diffusion through integral membrane proteins called aquaporins (Cooper, 2009). Diffusion of water through the cell is proportional to the surface area of the cell, and not necessarily constant. Likewise, aquaporins can be closed or open, and it is unlikely that they should remain in a certain position at all times.

Expanding the 2 models developed here could also possibly give some insight into how a significantly higher percentage of cancer cells manage to remain intact and resist bursting while withstanding tremendous hypotonic stresses. Perhaps they exert greater control over the aquaporins to regulate water entry, or their cytoskeleton is more rigid, enabling them to withstand higher stress without bursting.

Also, incorporating cytoskeletal action into these models would enable a more fundamental understanding of how different cancer cells behave differently from each other. Specifically, cancer behavior could be mapped to phenotype expressed along the EMT timeline. Mesenchymal phenotype cancer cells have been shown to correlate with increased metastatic potential (Yamada et al., 2013). This claim could be further supported and explained by comparing the mechanical characteristics of epithelial and mesenchymal cells. Such a correlation could allow a direct assessment of prognosis in patients from simple mechanical testing of CTCs.

The experiments here focused on differentiating the mechanical properties of cancer cells from other cells present in the blood. However, from a mechanobiology perspective, significant insight could be gained by repeating the experiments here with the benign counterparts of MCF7 and H661, which would be breast and lung tissue, respectively. Applying the expanded models described above could give an indication of the sort of mutations and abilities acquired by cancer cells that enables them to survive stresses and conditions that other cells would not be able to. It is these abilities that give cancer cells a much greater potential to metastasize to different areas of the body.

Chapter 5

Conclusion

Cancer is a leading cause of death around the world. Metastasis, the process whereby cancers spread to different parts of the body, causes 90% of cancer-associated deaths. Thus, recent research has focused on preventing metastasis by early cancer diagnosis and effective therapy regimens. Circulating tumor cells (CTC) are one promising emerging technology that fulfills these needs. CTCs are essentially tumor cells circulating in the blood that are shed by a primary tumor in the body. The detection, isolation, and characterization of CTCs can be used to in cancer diagnosis, prognosis, designing therapy schedules, and determining the efficacy of ongoing therapy. A principal mechanism that CTCs are isolated from blood is through their distinctive mechanical characteristics. They are both larger and more deformable than all other cells in the blood. While studies have used these characteristics to achieve a different purpose, few have characterized these in relation to the other cells. Also, most mechanisms used to characterize cell mechanics do not focus on the phenomenon of membrane folding in relation to cell expansion.

The experimental tactic of introducing hypotonic stresses to cells and imaging their subsequent expansion has proven valuable in characterizing the dynamics of the cell as it expands over time. Cancer cells were, in general, found to be larger and substantially more deformable than WBCs, their closest counterparts in the blood. Interestingly, there was also a significant amount of variation among cancer cells. MCF7, a breast carcinoma, and H661, a lung carcinoma, exhibited significantly different survival rates when exposed to pure DI water, different percentage expansions, and different expansion curves. The WBCs studied were a subset of mononuclear cells (MNCs). Experimentally, it was determined that the MNCs studied were in

fact a combination of 2 subgroups: monocytes (large MNCs) and lymphocytes (small MNCs). These differences between cancer cells and WBCs support the concept of using mechanical variations to separate them from blood. Furthermore, the mechanical differences among cancer cells can possibly be used as a means to characterize their phenotypes, instead of relying on biological or chemical signals expressed for characterization. Two models were generated from theory and fit to the experimental data. The first treated the cell as a thin-walled sphere of viscoelastic material with a constant interior pressure. The second model examined the osmotic pressure gradient across the shell as the stress inducer, and combined it with an elastic restoring force working against the expansion. Both models fit the MCF7 and H661 plots reasonably well, and can mimic the trend of the expansion data of the MNCs to a certain extent. However, to better fit the models to MNC data, more experimental data is needed to account for the increased uncertainty associated with image processing of pictures of smaller cells. The models developed here could be expanded to account for the action of the cell cytoskeleton as well as for the presence of aquaporins on the membrane that control water flux in and out of the cell. Some cells were observed to go through a blebbing process as part of their expansion. Additional experiments examining the cytoskeleton structure throughout the cell expansion would give some insight into the membrane-cytoskeleton interactions that occur during expansion, and possibly explain what the blebbing behavior is reflective of.

The studies conducted show that cancer cells can increase in diameter by up to 60%, which enables them to navigate the body and metastasize to different areas. The data suggests that a significant part of this expansion is made possible by folds present in the membrane. These folds are present to a much larger extent in cancer cells than MNCs. Furthermore, the variability in survival and % expansion between MCF7 and H661 could possibly be correlated with the Epithelial vs. Mesenchymal phenotype expressed by each. Research has shown that a mesenchymal phenotype correlates with a higher metastatic potential (Yamada et al. 2013). Thus,

the mechanics of isolated CTCs could give an estimate as to the aggressivity of the cancer in question, enabling a more accurate prognosis to be made, and a more appropriate treatment plan to be developed.

Chapter 6

Appendices

Appendix A: Image Analysis MATLAB Code

ProcessImage function

```
function [ BWfinal] = processimage2(picture,fudgeFactor,numerode)

% image has to be with extension and between quoatation marks
% fudgefactor determines threshold filtering
% numerode is the number of smoothing cycles the image undergoes
after the
% initial one.

% image = tostring(picture);
% image_str = strcat(picture, '.tif');

% Reads initial picture file. Make sure it is in MATLAB folder

% if using text input, change I in list of inputs to 'picture'
and
% uncomment

I = imread(picture);

%%% Filters junk out of picture. degree of filtering depends on
defined
% threshold.

%%% if a specific portion of the image is required, use the below
line.

% figure, I = imcrop(I);
% close figure 1

[junk threshold] = edge(I, 'sobel');
```

```

BWs = edge(I,'sobel', threshold * fudgeFactor);

%%% linear structural elements created

se90 = strel('line', 3, 90);
se0 = strel('line', 3, 0);

%%% image is dilated

BWsdil = imdilate(BWs, [se90 se0]);

%%% Insert a column of zeros on left
% [rows columns numberOfColorBands] = size(BWsdil);
% numColsToInsert = 1;
% startingColumn = 1;
% BWsdil = [BWsdil(:, 1:startingColumn) zeros(rows,
numColsToInsert) BWsdil(:, startingColumn+1:end)];

%%% insert a row of zeros on top
% [rows columns numberOfColorBands] = size(BWsdil);
% numRowsToInsert = 1;
% startingRow = 1;
% BWsdil = [BWsdil(1:startingRow,:); zeros(numRowsToInsert,
columns); BWsdil(startingRow+1:end,:)];

%%% Adding a column makes image type double. Convert back to
binary

% BWsdil = im2bw(BWsdil,0.5);

%%% Removes objects on border. 4 is used to remove diagonal
connections

BWnobord = imclearborder(BWsdil, 4);

%%% Fills interior gaps

BWdfill = imfill(BWnobord, 'holes');

```

```

%%% smoothen object. imerode function can be used as much as
desired.

seD = strel('diamond',1);
BWfinal = BWdfill;
k = 0;

while k< numerode

BWfinal = imerode(BWfinal,seD);
k=k+1;

end

% at any point above, if the image desired is to be shown use the
following
% command: figure, imshow(name_of_latest_modified_image)

figure,imshow(BWfinal)

% only needed if 2 cells touching each other
% BWfinal = bwmorph(BWfinal,'hbreak')
% figure,imshow(BWfinal)

end

```

GetArea Function

```

function [ areas ] = getArea(bw,num )

% receives bw image and num of areas desired. This is in line
% with visually
% verifying the number of areas desired. Num must be >=1.

area = regionprops(bw,'Area');
area=struct2cell(area);
area = cell2mat(area);

areas = zeros(1,num);

% area is the array of all areas in the picture

area_copy = area;
max_indices=[];
for k=1:num
    [maximum,I] = max(area);
    % areas(k) = maximum;
    area(I) = 0;
    max_indices(k)=I;
end

% sort max_indices array to ascending order.
max_indices = sort(max_indices);
for k=1:num
    areas(k)=area_copy(max_indices(k));
end

minimum = min(areas);

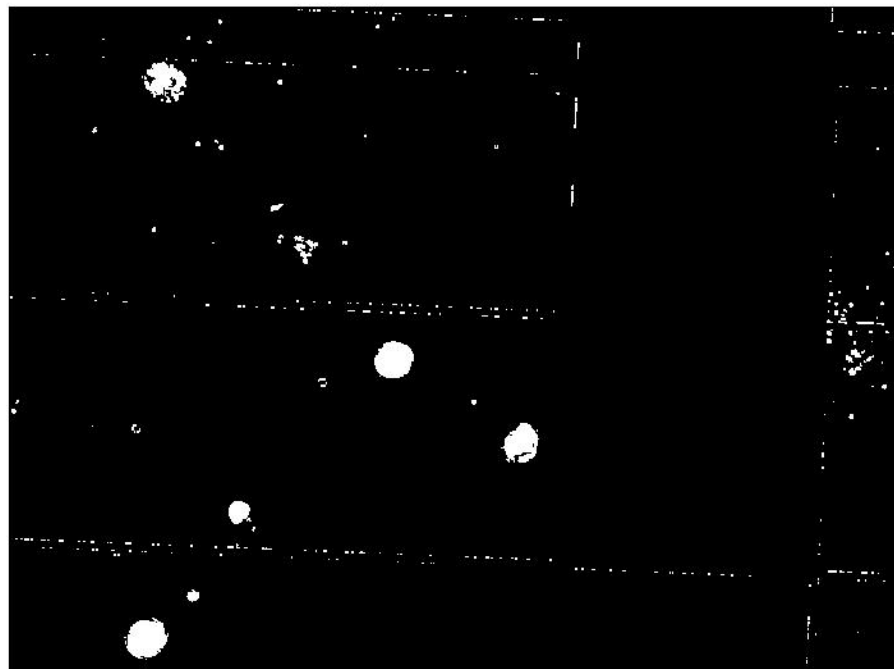
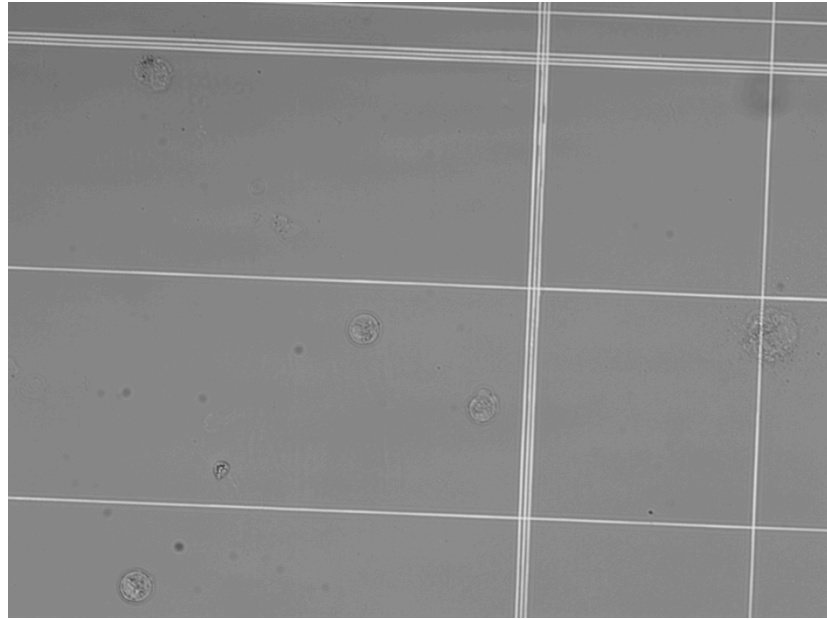
figure, imshow(bwareaopen(bw, minimum-10))

% this is to show the new image with only the selected areas

```

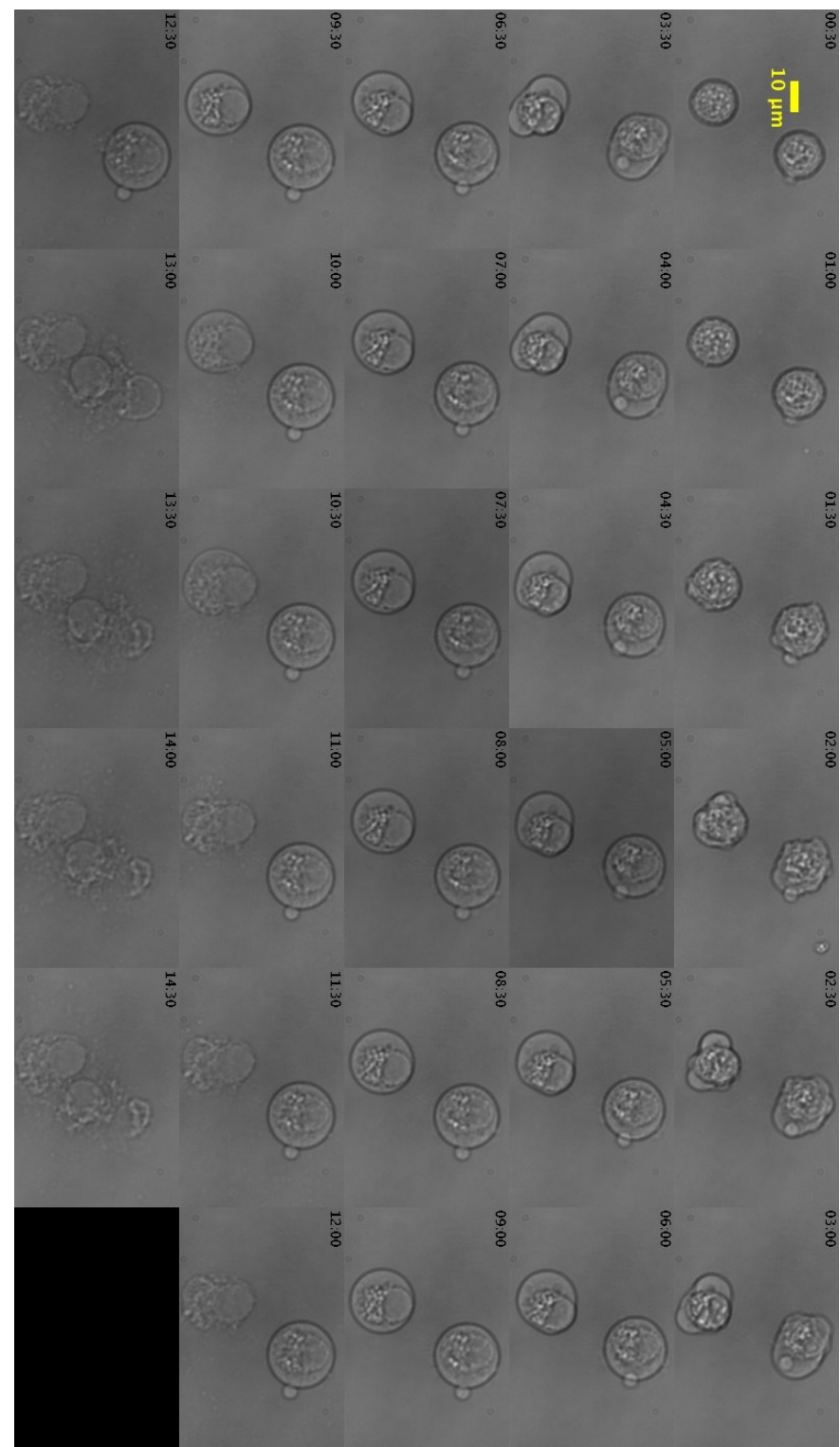
```
% size_cut = max(areas);  
%  
% imshow(bwareaopen(bw,size_cut));  
  
end
```


Example of binary image generated from experimental image using above code:



Appendix B: Cell Expansion Images

H661 Cells



MCF7 Cells



BIBLIOGRAPHY

- Abkarian, M., Faivre, M., & Stone, H. A. (2006). High-speed microfluidic differential manometer for cellular-scale hydrodynamics. *Proceedings of the National Academy of Sciences of the United States of America*, 103(3), 538–42. doi:10.1073/pnas.05071711102
- Charras, G., & Paluch, E. (2008). Blebs lead the way: how to migrate without lamellipodia. *Nature reviews: Molecular cell biology*, 9(9), 730–6. doi:10.1038/nrm2453
- Cooper, G. M., & Hausman, R. E. (2009). *The cell: a molecular approach* (5th ed.). Washington, D.C.: ASM Press ;.
- Cross, S. E., Jin, Y.-S., Rao, J., & Gimzewski, J. K. (2007). Nanomechanical analysis of cells from cancer patients. *Nature nanotechnology*, 2(12), 780–3. doi:10.1038/nnano.2007.388
- Di Carlo, D. (2012). A mechanical biomarker of cell state in medicine. *Journal of laboratory automation*, 17(1), 32–42. doi:10.1177/2211068211431630
- Fletcher, D. a, & Mullins, R. D. (2010). Cell mechanics and the cytoskeleton. *Nature*, 463(7280), 485–92. doi:10.1038/nature08908
- Friedl, P. & Wolf, K. Tumour-cell invasion and migration: diversity and escape mechanisms. *Nature Rev. Cancer* **3**, 362–374 (2003).
- Hallett, M. B., & Dewitt, S. (2007). Ironing out the wrinkles of neutrophil phagocytosis. *Trends in cell biology*, 17(5), 209–14. doi:10.1016/j.tcb.2007.03.002
- Harouaka, R. a, Nisic, M., & Zheng, S.-Y. (2013). Circulating tumor cell enrichment based on physical properties. *Journal of laboratory automation*, 18(6), 455–68. doi:10.1177/2211068213494391
- Ho, B. P., & Leal, L. G. (1974). Inertial migration of rigid spheres in two-dimensional unidirectional flows. *Journal of Fluid Mechanics*, 65(02), 365–400. doi:10.1017/S0022112074001431
- Hochmuth, R. M. (2000). Micropipette aspiration of living cells. *Journal of biomechanics*, 33(1), 15–22. Retrieved from <http://www.ncbi.nlm.nih.gov/pubmed/10609514>
- Hoshino, K., Huang, Y.-Y., Lane, N., Huebschman, M., Uhr, J. W., Frenkel, E. P., & Zhang, X. (2011). Microchip-based immunomagnetic detection of circulating tumor cells. *Lab on a chip*, 3449–3457. doi:10.1039/c1lc20270g
- Hou, H. W., Li, Q. S., Lee, G. Y. H., Kumar, a P., Ong, C. N., & Lim, C. T. (2009, June). Deformability study of breast cancer cells using microfluidics. *Biomedical microdevices*. doi:10.1007/s10544-008-9262-8

- Huang, L. R., Cox, E. C., Austin, R. H., & Sturm, J. C. (2004). Continuous particle separation through deterministic lateral displacement. *Science (New York, N.Y.)*, 304(5673), 987–90. doi:10.1126/science.1094567
- Hur, S. C., Henderson-MacLennan, N. K., McCabe, E. R. B., & Di Carlo, D. (2011). Deformability-based cell classification and enrichment using inertial microfluidics. *Lab on a chip*, 11(5), 912–20. doi:10.1039/c0lc00595a
- Kalluri, R., & Weinberg, R. A. (2009). Review series The basics of epithelial-mesenchymal transition. *The Journal of Clinical Investigation*, 119(6). doi:10.1172/JCI39104.1420
- Kufe, D., Pollock, R., Weichselbaum, R., Blast, R., Gansler, T., Holland, J., et al. (2003). The Government and Cancer Medicine. *Holland-Frei Cancer Medicine*(6th ed., p. N/A). Ontario: BC Decker.
- Lin, H., Balic, M., Zheng, S., Datar, R., & Cote, R. J. (2011). Disseminated and circulating tumor cells: Role in effective cancer management. *Critical reviews in oncology/hematology*, 77(1), 1–11. doi:10.1016/j.critrevonc.2010.04.008
- Maheswaran, S., & Haber, D. a. (2010). Circulating tumor cells: a window into cancer biology and metastasis. *Current opinion in genetics & development*, 20(1), 96–9. doi:10.1016/j.gde.2009.12.002
- McFaul, S. M., Lin, B. K., & Ma, H. (2012). Cell separation based on size and deformability using microfluidic funnel ratchets. *Lab on a chip*, 12(13), 2369–76. doi:10.1039/c2lc21045b
- Mehlen, P., & Puisieux, A. (2006). Metastasis: a question of life or death. *Nature reviews: Cancer*, 6(6), 449–58. doi:10.1038/nrc1886
- Mohandas, N., & Evans, E. (1994). Mechanical properties of the red cell membrane in relation to molecular structure and genetic defects. *Annu. Rev. Biophys. Biomol. Struct.*, 23, 787–818.
- Murphy, K. P., Travers, P., Walport, M., & Janeway, C. (2012). *Janeway's immunobiology* (8th ed.). New York: Garland Science.
- Nagrath, S., Sequist, L. V., Maheswaran, S., Bell, D. W., Irimia, D., Ulkus, L., Smith, M. R., et al. (2007). Isolation of rare circulating tumour cells in cancer patients by microchip technology. *Nature*, 450(7173), 1235–9. doi:10.1038/nature06385
- Robertson, A. M., Bird, C. C., Waddell, A. W. & Currie, A. R. Morphological aspects of glucocorticoid- induced cell death in human lymphoblastoid cells. *J. Pathol.* **126**, 181–187 (1978)

- Schmid-Schönbein, G. W., Shih, Y. Y., & Chien, S. (1980). Morphometry of human leukocytes. *Blood*, 56(5), 866–75. Retrieved from <http://www.ncbi.nlm.nih.gov/pubmed/6775712>
- Shim, S., Gascoyne, P., Noshari, J., & Hale, K. S. (2011). Dynamic physical properties of dissociated tumor cells revealed by dielectrophoretic field-flow fractionation. *Integrative biology: quantitative biosciences from nano to macro*, 3(8), 850–62. doi:10.1039/c1ib00032b
- Suresh, S. (2007). Biomechanics and biophysics of cancer cells. *Acta biomaterialia*, 3(4), 413–38. doi:10.1016/j.actbio.2007.04.002
- Talasaz, A. H., Powell, A. A., Huber, D. E., Berbee, J. G., Roh, K.-H., Yu, W., Xiao, W., et al. (2009). Isolating highly enriched populations of circulating epithelial cells and other rare cells from blood using a magnetic sweeper device. *Proceedings of the National Academy of Sciences of the United States of America*, 106(10), 3970–5. doi:10.1073/pnas.0813188106
- Voura, E. B., Sandig, M. & Siu, C. H. Cell–cell interactions during transendothelial migration of tumor cells. *Microsc. Res. Tech.* **43**, 265–275 (1998).
- Wang, L., Castro, C. E., & Boyce, M. C. (2011). Growth strain-induced wrinkled membrane morphology of white blood cells. *Soft Matter*, 7(24), 11319–11324. doi:10.1039/c1sm06637d
- Yamada, S., Fuchs, B. C., Fujii, T., Shimoyama, Y., Sugimoto, H., Nomoto, S., Takeda, S., et al. (2013). Epithelial-to-mesenchymal transition predicts prognosis of pancreatic cancer. *Surgery*, 154(5), 946–54. doi:10.1016/j.surg.2013.05.004
- Zheng, S., Liu, J., & Tai, Y. (2008). Streamline-Based Microfluidic Devices for Erythrocytes and Leukocytes Separation. *Journal of Microelectromechanical Systems*, 17(4), 1029–1038. doi:10.1109/JMEMS.2008.924274

ACADEMIC VITA:

Khalil B Ramadi

kbr5051@psu.edu

Current Address:

501 Vairo Blvd. Apt #1211
State College, PA 16803
(215) 353-0707

Permanent Address:

1924 Rittenhouse Square
Philadelphia, PA 19103

Education:

August 2010 – Present

The Schreyer Honors College, The Pennsylvania State University University Park, PA
B.S. in Mechanical Engineering & Bioengineering Expected: May 2014
Dean's list all semesters

September 2006 – June 2010

The International School of Choueifat Al-Ain, United Arab Emirates
High School Diploma (with Honors)

Honors & Awards:

- GRE Score: Verbal 165/170 (95th Percentile), Quantitative 167/170 (96th Percentile)
- NASA Aeronautics Scholarship, May 2011 - May 2013
- Harding Scholarship, Mechanical Eng. Dept., Penn State University, August 2013
- President's Freshman Award, Penn State University, March 2011
- NASA Pennsylvania Space Grant Consortium, Penn State University, December 2010

Experience:

<i>Sep 2013 – Present</i>	Mechanical Engineering Junior Design, Penn State University. Project: Design of a chaotic pendulum exhibit for the Discovery Space Children's museum in State College, PA. Driven by a need to combat the falling levels of interest in STEM fields expressed by the youth of America today.
<i>Jan 2013 – May 2013</i>	Bioengineering Junior Design, Penn State University. Project: Designing a microneedle patch for Measles vaccine delivery, considering the mechanism of action and large scale fabrication.
<i>May 2012 – Jul 2012</i>	Intern, Combustion branch, NASA Glenn Research Center. Cleveland, OH. Design of a novel liner for the Advanced Subsonic Combustion Rig
<i>Jan 2012 – Present</i>	Member, Micro & Nano Integrated Biosystem Laboratory Supervisor: Dr. S. Zheng, Dept. Bioengineering, Penn State University. Project: Examining cell membrane mechanics using BioMEMS

<i>May 2011</i>	Engineering Design Course, Ecole Centrale Nantes, France. Project: Designing a twist screw bottle cap opener for people with reduced dexterity in the hands.
<i>Jan 2011 – May 2011</i>	Freshman Engineering Design, Penn State University. Project: Design of a hydrogen gas station, and the possible large scale grid network implementation in the city of Los Angeles, CA. Group nominated for the best engineering design among 22 sections of the course.
<i>Dec 2010 – Dec 2011</i>	Member, Intense Laser Laboratory, Supervisor: Dr. Igor Jovanovic, Dept. Mechanical & Nuclear Engineering, Penn State University. NASA FURP (Freshman Undergraduate Research Program) scholarship. Project: Creating a LabView script to assist characterization of femtosecond laser pulses.
<i>Jun 2007/2008/2009</i>	Volunteer, Depts. Microbiology-Immunology & Physiology, UAE Univ. Research themes: Cancer immunotherapy Electrophysiology of gastrointestinal tract Nanoparticles for cancer therapy

Invited Presentations:

- ‘ASCR Thermal Liner Dynamics Evaluation, Revision, and Redesign’, Ideas in Flight Conference, NASA Headquarters, Washington DC, Jul 24-25, 2012.

Skills:

- Leadership experience, teamwork and communication – PSIDE (See Below)
- Multilingual: Native speaker of English, Spanish and Arabic
- Hands-on experience with Solidworks, MATLAB, LabView, Java, FEA, COMSOL and CFD.
- Practical experience with Lithographic Microfabrication techniques.

Extracurricular activities:

- PSIDE – Penn State International Dance Ensemble: Choreographer & Dancer
- Penn State Ballroom Dance Club – Latin Dancing Instructor